

Study of Baryon Stopping, Pion and Proton production
from 4.9 GeV Al + Au Fixed-Target Collisions at STAR

By

TODD ADLER KINGHORN
DISSERTATION

Submitted in partial satisfaction of the requirements for the degree of

DOCTOR OF PHILOSOPHY

in

Physics

in the

OFFICE OF GRADUATE STUDIES

of the

UNIVERSITY OF CALIFORNIA

DAVIS

Approved:

Daniel Cebra, Chair

Manuel Calderón de la Barca Sánchez

Ramona Vogt

Committee in Charge

2020

ProQuest Number:28089833

All rights reserved

INFORMATION TO ALL USERS

The quality of this reproduction is dependent on the quality of the copy submitted.

In the unlikely event that the author did not send a complete manuscript and there are missing pages, these will be noted. Also, if material had to be removed, a note will indicate the deletion.



ProQuest 28089833

Published by ProQuest LLC (2020). Copyright of the Dissertation is held by the Author.

All Rights Reserved.

This work is protected against unauthorized copying under Title 17, United States Code
Microform Edition © ProQuest LLC.

ProQuest LLC
789 East Eisenhower Parkway
P.O. Box 1346
Ann Arbor, MI 48106 - 1346

To my parents: Mom, thank you so much for your continuous support throughout my entire academic career. Dad, thank you for the many engaging and thought-provoking conversations we had related to math and physics.

CONTENTS

List of Figures	v
List of Tables	xi
Abstract	xii
Acknowledgments	xiii
1 Introduction	1
1.1 Hadronic matter and the Quark Gluon Plasma	1
1.2 The Beam Energy Scan Program at RHIC	4
1.3 The STAR Detector	6
1.4 Motivation	6
1.4.1 Baryon Stopping	8
2 STAR	10
2.1 Time Projection Chamber	10
2.1.1 Particle Identification	13
2.2 The Time of Flight	15
2.3 Why study asymmetric systems like Al+Au?	17
3 STAR Fixed-Target Al + Au 4.9 GeV Test Run	19
3.1 Setup	19
3.2 Fixed-Target Trigger	20
3.3 Event, Vertex, and Track Selection	22
4 Centrality Selection	27
5 Extracting the Raw Yields	32
6 Efficiency Corrections	38
7 Corrected Spectra	40
7.1 Overall Systematic Errors for the Spectral Points	40

8 Rapidity Density Yields	43
8.1 Results	43
8.2 Discussion of Systematic Uncertainties	45
8.3 Comparison to Published Data	48
8.3.1 π^- Rapidity Density comparison	48
8.3.2 Proton Rapidity Density comparison	49
9 Discussion of Baryon Stopping	52
10 Conclusion	62

LIST OF FIGURES

1.1	Almond shaped interaction volume from a non-central collision of two nuclei. The spatial anisotropy with respect to the reaction plane (the x - z plane) translates into a momentum anisotropy of the produced particles. From [1]	2
1.2	Measurements of elliptic flow (v_2) of various particle species from STAR and PHENIX. Hydrodynamic models agree well with observations below p_T of $\sim 1 - 2$ GeV/ c , evidence of a strongly coupled quark-gluon plasma. From [2]	3
1.3	QCD phase diagram cartoon showing the region accessible with the FXT program.	5
2.1	Schematic of STAR TPC (From [3])	11
2.2	Diagram of the side view of one of the outer sectors. (From [3])	12
2.3	A schematic of a single anode sector of the TPC. The inner portion of the sector is on the right and the outer is on the left. (From [3])	12
2.4	Energy loss (KeV/cm) as a function of momentum over charge (GeV/ c) in the Time Projection Chamber. The bands correspond to different particles and charges.	14
2.5	Side view of MRPC module (From [4])	15
2.6	Prototype design of schematic of a single TOF tray with projectively arranged MRPCs. (From [5])	16
2.7	Inverse velocity as a function of momentum over charge (GeV/ c) in the Time of Flight detector. The bands correspond to different particles of mass and charge.	16
2.8	The event display for Al + Au collisions at $\sqrt{s_{NN}} = 4.9$ GeV.	17
2.9	Asymmetric collision cartoon representing participants from both nucleons	18

3.1	(a) A schematic of the 2015 Fixed-Target Au + Au test run. The incident Au beam enters the TPC from the West side (which is on the right side of this figure, the arrow pointing toward the fixed-target) and is eventually aimed to skim the top of the target, located 211 cm West of the center of the detector. (b) The gold foil target of height 1 cm, width 4 cm, and thickness 1 mm.	20
3.2	TOF multiplicity with event level cuts for Al + Au runs at $\sqrt{s_{NN}} = 4.9$ GeV. As can be seen in Table 3.1, the TOF multiplicity cut thresholds are visible at TOF multiplicity cuts of 25 and 40.	22
3.3	(a) The full set of reconstructed vertices. The Au target is located at $V_z = 211$ cm, as shown by the vertical dashed line. (b) The $V_x - V_y$ distribution of reconstructed vertices in the vicinity of the target prior to event selection cuts.	24
3.4	(a) The V_z distribution of reconstructed vertices after event selection cuts. The Au target is located at $V_z = 211$ cm. (b) The $V_x - V_y$ distribution of reconstructed vertices after event selection cuts.	24
4.1	A cartoon showing the overlap region for a collision between an aluminum nucleus and a gold nucleus at different centralities. For more central collisions, the aluminum nucleus is engulfed by the gold nucleus.	27

4.2	The centrality selection for the STAR FXT Al + Au collisions at $\sqrt{s_{NN}} = 4.9$ GeV. The centrality variable depends on the number of tracks that pass track quality assurance cuts. The distribution of events with a given multiplicity of good tracks is shown with solid black circles. The blue curve is the Glauber Monte-Carlo + Negative Binomial fit to the data. The red dashed curve is a Monte-Carlo model of pile-up events. The black dashed lines show the centrality selection lines for top 30%, 25%, 20%, 15 %, 10%, and 5%. In addition, a dashed black line is shown at a multiplicity of 125, which illustrates the high multiplicity pile-up cut; events with greater than this multiplicity were most likely to have resulted from two Al + Au collisions within the target during the same beam bunch and were excluded from this analysis.	30
5.1	Fixing of the pion width parameter in double Gaussian fit for pion yield. This is done for each centrality, rapidity, and $m_T - m_0$. This fit is a piecewise polynomial.	33
5.2	Fixing of the electron width parameter in double Gaussian fit for pion yield. This is done for each centrality, rapidity, and $m_T - m_0$. This fit is a piecewise polynomial.	34
5.3	Fixing of the electron amplitude parameter in double Gaussian fit for pion yield. This is done for each centrality, rapidity, and $m_T - m_0$. The values at each bin are used.	34
5.4	The z_{TPC} fit of the pions (brown dashes) and electrons (purple dashes) for the 0-5% centrality bin, beam rapidity $y = -1.1$, and $m_T - m_0 = 65$ MeV bin.	35
5.5	The z_{TOF} fit of the protons (green dashes), pions (brown dashes), kaons (blue dashes), and deuterons (blue-green dashes) for the 0-5% centrality bin, beam rapidity $y = -1.1$, and $m_T - m_0 = 65$ MeV bin. Plot created by Sam Heppelmann.	36

5.6	The z_{TPC} fit of the protons (green dashes) and pions (brown dashes) for the 0-5% centrality bin, beam rapidity $y = -1.1$, and $m_T - m_0 = 65$ MeV bin. Plot created by Sam Heppelmann.	37
6.1	The efficiency fit to the ratio of matched tracks to embedded tracks for an example rapidity bin.	39
7.1	The yield ratio for pions rapidity slices equally spaced backward and forward of mid-rapidity for the 3.0 GeV Au+Au FXT system. These data are from the 2018 run. Physics requires the pion yields to be symmetric around mid-rapidity. Therefore the value of the backward/forward ratio is a measure of the systematic error in the efficiency correction. The systematic error in the efficiency correction is found to be 5% for higher $m_T - m_0$ bins.	41
8.1	Invariant spectra of π^- for different rapidity and centrality classes from STAR FXT Al+Au collisions at $\sqrt{s_{NN}} = 4.9$ GeV. To make the plot more legible, the spectra are scaled by a factor of $3.5^{\pm n}$, where n is 0 for target-rapidity and increases by one for each successive rapidity slice (the rapidity are quoted in the laboratory frame). The data are fit with a double Bose-Einstein function. The fit function is displayed as a solid line where there are data and as a dashed line where extrapolated to low $m_T - m_0$	44
8.2	Invariant spectra of protons for different rapidity centrality classes from STAR FXT Al+Au collisions at $\sqrt{s_{NN}} = 4.9$ GeV. To make the plot more legible, the spectra are scaled by a factor of $5^{\pm n}$, where n is 0 for mid-rapidity. The data are extrapolated to low $m_T - m_0$ with a thermal fitting function.	45
8.3	π^- rapidity density distributions for different centrality bins from Al+Au collisions at $\sqrt{s_{NN}} = 4.9$ GeV. The systematic error bars (yellow bars) are only shown for the 0-5% centrality bin; the relative errors for the other centralities are similar.	46

8.4	Proton rapidity density distributions for different centrality bins from Al+Au collisions at $\sqrt{s_{NN}} = 4.9$ GeV from STAR. Three Gaussians are used to fit the protons. One Gaussian describes the spectator protons from the Au target, another describes the participant protons from the Au target, and the last represents the participant protons from the Al projectile.	47
8.5	A comparison of the π^- rapidity density distribution (0-5%) with collisions at $\sqrt{s_{NN}} = 5.4$ GeV from the E802 (Si+Au, 0-7%) [6] and E810 (Si+Pb, 0-9%) [7, 8] experiments at the AGS. Systematic errors are shown as yellow bars.	50
8.6	Comparison of the proton rapidity density distributions with (0-7%) Si+Au collisions at $\sqrt{s_{NN}} = 5.4$ GeV from E802 [6]. Systematic errors are shown as yellow bars.	51
9.1	π^- rapidity density distributions for 0-5% centrality from Al+Au collisions at $\sqrt{s_{NN}} = 4.9$ GeV.	53
9.2	π^- rapidity density distributions for 5-10% centrality from Al+Au collisions at $\sqrt{s_{NN}} = 4.9$ GeV.	53
9.3	π^- rapidity density distributions for 10-15% centrality from Al+Au collisions at $\sqrt{s_{NN}} = 4.9$ GeV.	54
9.4	π^- rapidity density distributions for 15-20% centrality from Al+Au collisions at $\sqrt{s_{NN}} = 4.9$ GeV.	54
9.5	π^- rapidity density distributions for 20-25% centrality from Al+Au collisions at $\sqrt{s_{NN}} = 4.9$ GeV.	55
9.6	π^- rapidity density distributions for 25-30% centrality from Al+Au collisions at $\sqrt{s_{NN}} = 4.9$ GeV.	55
9.7	Proton rapidity density distributions for 0-5% centrality from Al+Au collisions at $\sqrt{s_{NN}} = 4.9$ GeV. The solid line represents the triple Gaussian fit. The dashed lines represent the individual Gaussians fits that correspond to the Au target spectator protons, Au target participant protons, and Al beam participant protons.	56

9.8	Proton rapidity density distributions for 5-10% centrality from Al+Au collisions at $\sqrt{s_{NN}} = 4.9$ GeV. The solid line represents the triple Gaussian fit. The dashed lines represent the individual Gaussians fits that correspond to the Au target spectator protons, Au target participant protons, and Al beam participant protons.	57
9.9	Proton rapidity density distributions for 10-15% centrality from Al+Au collisions at $\sqrt{s_{NN}} = 4.9$ GeV. The solid line represents the triple Gaussian fit. The dashed lines represent the individual Gaussians fits that correspond to the Au target spectator protons, Au target participant protons, and Al beam participant protons.	57
9.10	Proton rapidity density distributions for 15-20% centrality from Al+Au collisions at $\sqrt{s_{NN}} = 4.9$ GeV. The solid line represents the triple Gaussian fit. The dashed lines represent the individual Gaussians fits that correspond to the Au target spectator protons, Au target participant protons, and Al beam participant protons.	58
9.11	Proton rapidity density distributions for 20-25% centrality from Al+Au collisions at $\sqrt{s_{NN}} = 4.9$ GeV. The solid line represents the triple Gaussian fit. The dashed lines represent the individual Gaussians fits that correspond to the Au target spectator protons, Au target participant protons, and Al beam participant protons.	58
9.12	Proton rapidity density distributions for 25-30% centrality from Al+Au collisions at $\sqrt{s_{NN}} = 4.9$ GeV. The solid line represents the triple Gaussian fit. The dashed lines represent the individual Gaussians fits that correspond to the Au target spectator protons, Au target participant protons, and Al beam participant protons.	59
9.13	Mean π^- and proton y_{lab}/y_{beam} as a function of centrality. The black line is the calculation of the mean interaction zone rapidity, y_{IZ}/y_{beam} , as a function of centrality from Table 9.1.	61

LIST OF TABLES

3.1	The number of bunches, minimum TOF Multiplicity cut, number of triggers, number of vertices, and efficiency for each run number as well as the total for Al + Au runs at $\sqrt{s_{NN}} = 4.9$ GeV.	21
4.1	The centrality bins used in the analyses. Included are the average number of participating nucleons (N_{part}) for each centrality class, as well as the break down of how many of those nucleons were contributed by the aluminum projectile and how many were contributed by the gold target as calculated using a Glauber Monte Carlo model. Each bin corresponds to 5% of the total cross section.	31
7.1	Sources of systematic uncertainty	42
9.1	Mean $y_{\text{lab}}/y_{\text{beam}}$ of the Gaussian fit to the dN/dy distributions for pions (μ_{π^-}) and protons (μ_p) for different centralities. The y_{IZ}/y_{beam} represents the fraction of the interaction zone rapidity to the beam rapidity.	60

ABSTRACT

Study of Baryon Stopping, Pion and Proton production from 4.9 GeV Al + Au Fixed-Target Collisions at STAR

One of the goals of the Relativistic Heavy Ion Collider (RHIC) Beam Energy Scan program is to explore whether signatures of the quark-gluon plasma can be turned off, search for a potential Quantum-Chromodynamic (QCD) critical point, as well as identify the phase transition between hadronic and partonic matter. This program ran from the years 2010 through 2014 and certain observables such as the directed flow of protons and higher moments of net-protons show features that may suggest some sort of transition to hadron-dominated matter below 20 GeV.

The Solenoidal Tracker at RHIC (STAR) Fixed-Target program was created to extend center of mass energies below $\sqrt{s_{NN}} = 7.7$ GeV, down to $\sqrt{s_{NN}} = 3.0$ GeV, as these energies are not practical to do with colliding beams at RHIC. This will be crucial in the second phase of the Beam Energy Scan program, BES-II, as data from energies within this range may yield information of the phase transition. The capabilities of reconstructing interactions with a fixed-target geometry needed to be demonstrated for the future of the program in BES-II. In 2015, two test runs with a fixed-target geometry were done with the STAR detector; the first was Au + Au at $\sqrt{s_{NN}} = 4.5$ GeV and the second, a month later, was Al + Au at $\sqrt{s_{NN}} = 4.9$ GeV center-of-mass energy.

This dissertation focuses on the asymmetric Al + Au collisions but will involve mentions of the Au + Au run. In this work, the spectra and rapidity density of π^- and p are measured at the top 0-5%, 5-10%, 10-15%, 15-20%, 20-25%, and 25-30% most central collisions. In addition, the “stopping” for protons will be discussed.

ACKNOWLEDGMENTS

To my advisor, Daniel: thank you for being a great mentor, instructor, and for always being available to discuss any topic. I enjoyed our general conversations. With your guidance and patience, I thank you for my progression in data analysis techniques. I enjoyed the time we spent working together during my travel at STAR.

Manuel, thank you for introducing me to the NPG many years ago. I am grateful for the many questions you have asked me over the years about anything I showed during group meeting. I appreciate being able to ask you about anything related to physics or otherwise.

Kathryn and Chris, thank you both for helping me with many of my physics and programming questions. I am grateful for the effort you both put in to helping me, especially at the beginning. Much of what I have learned has come from the both of you.

To the members of my dissertation committee: Daniel, Manuel, and Ramona: thank you for your taking the time to catch the many errors I had. My dissertation is now in a much better state than it originally was.

To everyone in NPG, thank you. The entire group has been extremely supportive and incredibly friendly. To Sam, Ben, Matt, and Zach, you are all doing well in each of your careers and I hope the rest of each of your programs continue to go well. To Ota, thank you for the many seemingly random conversations we had in the office. To Vincent, thank you for your quick response time for the many technical issues I had. To Jared, Graham, and Heather, I have enjoyed the discussions we had over the years. I will miss the group barbecues and the times we all went out to various restaurants for celebrations.

To my parents: Mom, thank you again for your support throughout the many, many years of school. Without your support, none of this would have been possible. Dad, thank you again for always wanting to discuss anything related to math, physics, and other sciences. Your interest in these many topics furthered my interest in the field.

To Bob and Tina, thank you both for your support. Bob, much of my early interest in computers and technology comes from you and I thank you for that. Tina, thank you for always checking in on me and asking if I had time for activities outside of academia.

Chapter 1

Introduction

1.1 Hadronic matter and the Quark Gluon Plasma

In 1973, asymptotic freedom was discovered by D. Gross, H. D. Politzer, and F. Wilczek [9–12]; they discovered that the interaction between quarks changes inversely with the scale of energy. That is, at low energies, the interaction between quarks is stronger, leading to the confinement of quarks within a hadron. Conversely, at higher energies, the interaction between quarks is weaker. In 2004, these three researchers shared a Nobel Prize for their discovery.

In 1994, a heavy-ion program at the Super-Proton-Synchrotron (SPS) collider at CERN began with the purpose of colliding heavy ions at energies high enough to create energy densities extreme enough for quarks to become deconfined. In 2000, evidence of a new state of matter that consisted of deconfined quarks had been observed [13]. However, there was still debate over whether or not this new state of matter was the predicted quark-gluon plasma (QGP). The properties of this plasma are sought after as they allow for the study of the strong force, and therefore, Quantum-Chromodynamics (QCD), which is has to do with the strong interaction between quarks and gluons. Also, in this same year, the Relativistic Heavy Ion Collider (RHIC) located in Brookhaven National Laboratory (BNL) in Upton, New York, had their first data-taking runs. The top energy of SPS for lead ions was a $\sqrt{s_{NN}}$ of 17 GeV. The top energy for RHIC is a $\sqrt{s_{NN}}$ of 200 GeV for gold ions. BNL released a report containing results from the first

four experiments, PHOBOS, STAR, PHENIX, and BRAHMS. The report confirmed the observation of a QGP [14]. It is discussed in this report that the QGP observed was more strongly coupled than expected and behaved like a nearly perfect fluid. In 2010, the Large Hadron Collider (LHC) at CERN started taking data for their heavy-ion program. The LHC first collided lead ions at a $\sqrt{s_{NN}}$ of 2.76 TeV. Though the energy at the LHC was much higher than that at RHIC, the initial results agreed with RHIC [15]. Though there are many things that describe the QGP state of matter, one such piece is called “flow”. Flow signals the presence of multiple interactions between the constituents of the medium created in the collision [1].

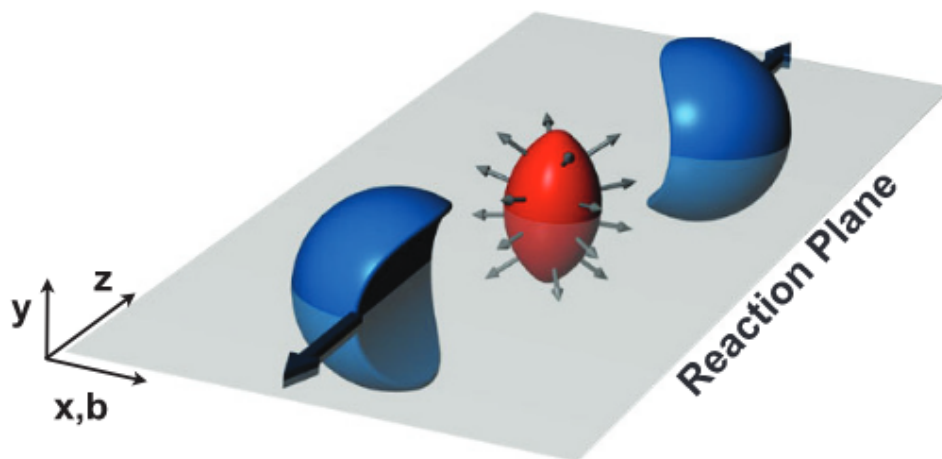


Figure 1.1: Almond shaped interaction volume from a non-central collision of two nuclei. The spatial anisotropy with respect to the reaction plane (the x - z plane) translates into a momentum anisotropy of the produced particles. From [1]

As the number of interactions increase, this usually leads to a larger magnitude of flow and the system is brought closer to thermalization [1]. A way to experimentally discuss evidence of flow is from the observation of the anisotropic flow. This is the anisotropy in the particle momentum distributions correlated to the reaction plane. The reaction plane is defined by the beam axis and the vector connecting the centers of the two colliding nuclei. The anisotropic flow can be described in a Fourier expansion,

$$E \frac{d^3N}{d\mathbf{p}^3} = \frac{1}{2\pi} \frac{d^2N}{p_T dp_T dy} \left(1 + 2 \sum_{n=1}^{\infty} v_n \cos[n(\phi - \Psi_{RP})] \right) \quad (1.1)$$

where E is the energy of the particle, p the momentum, p_T the transverse momentum (momentum perpendicular to the beam axis), ϕ the azimuthal angle of the emitted particle, y the rapidity, v_n are the Fourier coefficients, and Ψ_{RP} the reaction plane angle. The sine terms in this expansion vanish because ϕ is symmetric with respect to the reaction plane. Figure 1.1 is a cartoon example of a non-central interaction of two nuclei. In this example, the reaction plane is the x - z plane. The rapidity is defined as

$$y = \frac{1}{2} \ln \left(\frac{E + p_z}{E - p_z} \right) \quad (1.2)$$

where p_z is the direction of the beam axis. The Fourier coefficients can be written as,

$$v_n = \langle \cos n(\phi - \Psi_{RP}) \rangle \quad (1.3)$$

where the angle brackets indicate an average over all particles of interest, and n denotes the harmonic. The first harmonic is called directed flow (v_1) and the second is called elliptic flow (v_2). Figure 1.2 plots the elliptic flow as a function of p_T for various particle species, as

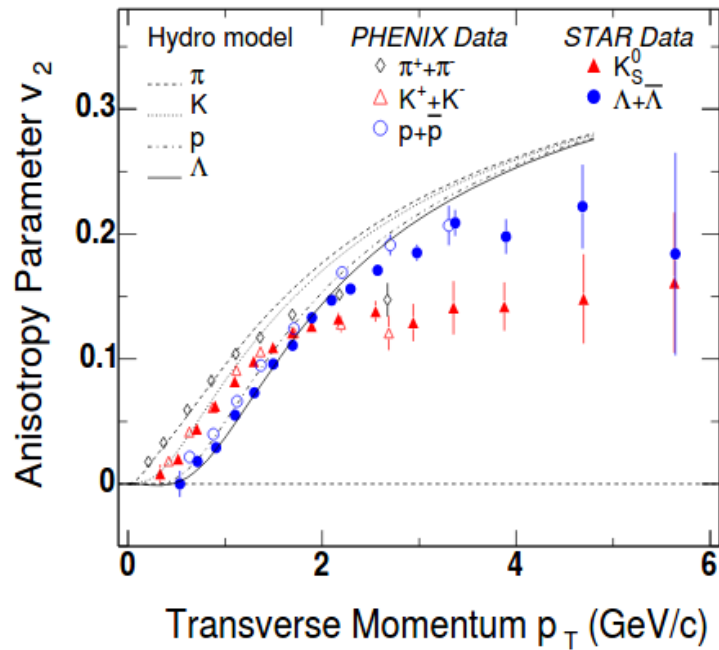


Figure 1.2: Measurements of elliptic flow (v_2) of various particle species from STAR and PHENIX. Hydrodynamic models agree well with observations below p_T of $\sim 1 - 2$ GeV/ c , evidence of a strongly coupled quark-gluon plasma. From [2]

measured by STAR and PHENIX. In addition, hydrodynamic models for various particle

species are included. The hydrodynamic models agree well with observations below p_T of $\sim 1 - 2$ GeV/c, evidence of a QGP. At higher p_T , the hydrodynamic models do not agree. This is due to incomplete equilibrium at high p_T [16].

1.2 The Beam Energy Scan Program at RHIC

The Relativistic Heavy Ion Collider is located in Brookhaven National Laboratory in Upton, New York. It is the first synchrotron able to collide heavy ions and began operations in the year 2000. The facility at RHIC houses a complex accelerator that has the capability to bring various nuclei to relativistic speeds. The circumference of RHIC is 3.8 km and the collider is designed to be able to have collisions at up to a center of mass energy ($\sqrt{s_{NN}}$) of 200 GeV for Au+Au and up to $\sqrt{s_{NN}} = 500$ GeV collisions for $p + p$. These energies allow for high temperature systems necessary to study the properties of the QGP. At these energies, as the QGP cools, it transitions to a hadron gas through a crossover transition [17] at approximately a temperature of 155 MeV [18]. A crossover transition is defined as having no discontinuities in the thermodynamic state variables as well as having no discontinuities in any of their derivatives. A first order phase transition implies a discontinuity in one (or more) of the state variables. If there exists a first order phase transition, then there should exist a critical point that connects the two types of phase transitions [19–21]. At a critical point, there is no longer any way to distinguish between the two phases.

Figure 1.3 shows a cartoon QCD phase diagram with temperature plotted against baryon chemical potential (μ_B). The baryon chemical potential describes the balance of matter to anti-matter. The case of a balance between matter and anti-matter is if $\mu_B = 0$. If $\mu_B > 0$, then there is more matter than anti-matter. If $\mu_B < 0$, then there is more anti-matter than matter. The LHC and the top energy of RHIC probe the phase diagram at values of μ_B close to zero, However, the RHIC collider is capable of colliding energies as low as a $\sqrt{s_{NN}}$ of 7.7 GeV in a collider configuration. This energy range allows for RHIC to be able to reach higher μ_B values (baryon rich) and therefore allows for the search of multiple features of the phase diagram such as the first order phase transition

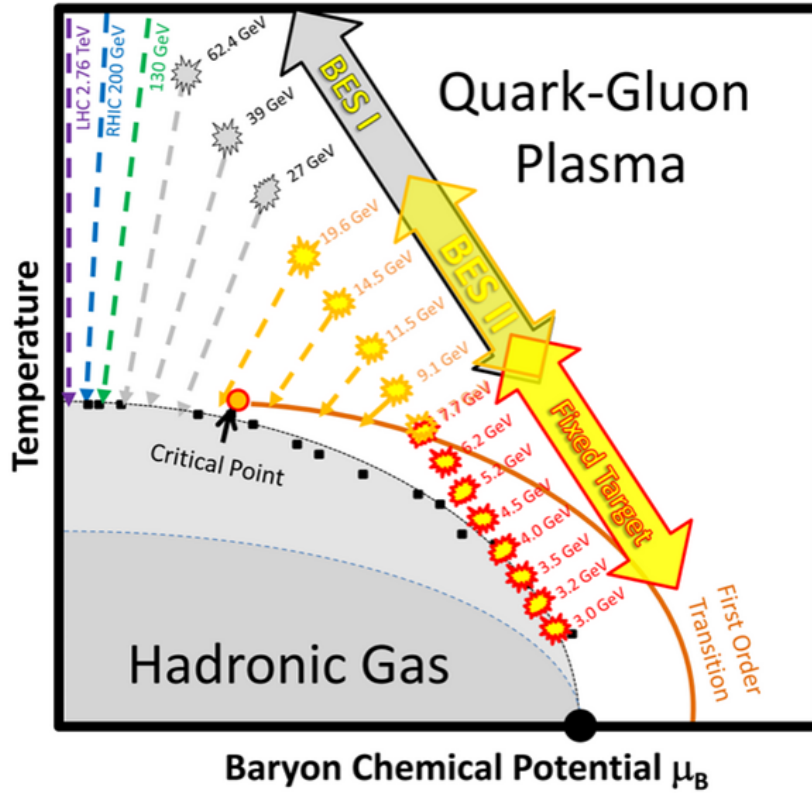


Figure 1.3: QCD phase diagram cartoon showing the region accessible with the FXT program.

and a critical point. In 2010, the Beam Energy Scan (BES) program ran from 2010-2014 and collided gold ions at energies of $\sqrt{s_{NN}} = 62.4, 39, 27, 19.6, 14.5, 11.5,$ and 7.7 GeV.

This dissertation covers a study at a collision energy of $\sqrt{s_{NN}} = 4.9$ GeV, which is quite a bit lower than the design energy of the collider, a different mode was setup for taking data. First, it should be noted that runs during the Beam Energy Scan (BES-I) Program demonstrated that the luminosity drastically drops with $\sqrt{s_{NN}}$ and, as such, energies below $\sqrt{s_{NN}} = 7.7$ GeV require a very long time for data taking – to a point which becomes impractical. The luminosity (\mathcal{L}) is defined as,

$$\mathcal{L} = \frac{1}{\sigma} \frac{dN}{dt} \quad (1.4)$$

where σ is the interaction cross-section, N is the number of events detected within some time interval. As $\sqrt{s_{NN}}$ drops, it becomes increasingly challenging to focus the beam due to the Coulomb repulsion between the positively charged ions, which causes the beam

to spread. However, in a fixed-target configuration, where a single beam collides with a target fixed in place, lower $\sqrt{s_{NN}}$ energies become accessible with high rates, down to $\sqrt{s_{NN}}$ of 3.0 GeV. In this fixed-target configuration it was possible to collect order 10^6 events in a time frame of an order of an hour. To obtain equivalent statistics at these lower center of mass energies in a collider configuration, a time frame many orders of magnitude longer would have been required.

1.3 The STAR Detector

The Solenoidal Tracker at RHIC (STAR) detector [22] is made up of many, many subdetectors that are used by the STAR Collaboration for the study of heavy-ion collisions. As time has passed, parts of the detectors have been replaced, upgraded, added, removed, etc. in order to keep pace with the physics goals and requirements of the STAR Collaboration. Particle identification and tracking are a necessity for the experiments and measurements that are performed at STAR. The Time Projection Chamber (TPC) provides tracking and particle identification and the Time of Flight (TOF) provides additional particle identification at higher momenta than the TPC. It is these two subdetectors that are primarily involved in this dissertation and analysis. These will be discussed in Chapter 2.

1.4 Motivation

The Beam Energy Scan program at RHIC was designed to study the nature of the phase transition between the hadronic and partonic phases of nuclear matter. In particular, it was proposed to search for the critical point between the two phases and to identify features of a softening of the equation of state consistent with a first order phase transition. There are several lines of analysis which suggest that deconfinement has been achieved in the low energy range of the BES-I. Most notably, the higher moments of the net-proton multiplicity distributions show an enhancement at 7.7 GeV which is consistent with the predictions for critical behavior [23, 24]. The K^+/π^+ ratio was seen to peak at 7.7 GeV by the NA49 experiment [25]; this result is confirmed by the STAR BES-I data [26]. The directed flow of net protons shows a transition from positive to negative flow which is consistent with a softening of the equation of state expected in the spinodal region

created by a first order phase transition [27]. The correlations attributed to the chiral magnetic effect, which is expected to be associated with deconfined matter, are observed down to 7.7 GeV [28]. Similarly, the balance functions show features consistent with deconfined matter down to 7.7 GeV [29]. The importance of studying collision energies as low as possible has long been recognized. The first version of the BES proposal, in the 2007 BUR [30], requested energies of 4.6 and 6.3 GeV. The BES-I proposal, in the 2009 Beam Use Request (BUR), requested 500,000 events at 5.0 GeV. This request was taken seriously by the Collider-Accelerator Department (CAD) and test runs at 5.5 GeV and 5.0 GeV were performed in 2009 and 2010 respectively. Unfortunately they were unable to circulate beams at 5.5 GeV in 2009, and even though they were able to correct for the non-linearities of the arc dipole magnets and circulate beams at 5.0 GeV in 2010, the luminosity was so low that STAR was able to record only a single Au + Au collision during the course of that test.

The study of collisions below 7.7 GeV is not practical using RHIC in “collider mode.” Nevertheless, it is still extremely important. Fortunately, it is possible to study systems with a center-of-mass energy between $\sqrt{s_{NN}} = 3.0$ and $\sqrt{s_{NN}} = 7.7$ GeV using fixed-target (FXT) collisions (see Figure 1.3). Note that in theory the beams developed for $\sqrt{s_{NN}} = 5.0$ GeV collisions could be used to generate fixed-target data with a center of mass energy as low as 2.5 GeV, however it is expected that circulating a beam at this energy will take a significant amount of accelerator beam development time, therefore a $\sqrt{s_{NN}} = 3.0$ GeV is currently considered to be the lowest practical FXT energy. The current fixed-target program using an internal gold target was motivated by earlier studies of collisions between the gold ions in the beam halo and aluminum nuclei in the beam pipe during the BES program in 2010 and 2011. The internal gold target was installed in 2014 and a few thousand beam halo collisions were recorded during the 14.5 GeV collider run ($\sqrt{s_{NN}} = 3.9$ GeV). There was some doubt as to the make-up of the beam halo, therefore in 2015 a short test run was performed to graze the upper edge of the internal target with beams circulating at injection energy ($\sqrt{s_{NN}} = 4.5$ GeV). Another test run was performed by inserting an Al beam and guiding the beam to hit the gold target at $\sqrt{s_{NN}} = 4.9$ GeV.

These test runs were successful and 1.3 million events were recorded for the Au + Au FXT test run and 3.4 million events were recorded for the Al + Au FXT test run. This is a large enough data set to do several physics analyses. This dissertation is dedicated to the Al + Au FXT collisions at $\sqrt{s_{NN}} = 4.9$ GeV. Si + Au collisions at comparable energies had been studied in the 1990's during the AGS heavy-ion program that preceded RHIC. The analyses described in this dissertation demonstrate the capabilities of the FXT program at STAR by reproducing many of the key results from the AGS heavy-ion program, and, where possible, extending those measurements.

The results of the Al+Au $\sqrt{s_{NN}} = 4.9$ GeV can be compared to previous existing measurements of similar systems and energies. The Alternating Gradient Synchrotron (AGS) heavy ion program used $\sqrt{s_{NN}} = 5.4$ GeV silicon beams from 1992 to 1998. Results are available for π^- and protons from 0-7% centrality Si+Au collisions from the E802 experiment [6, 31, 32] and π^- and protons from the 0-9% centrality Si+Pb collisions from the E810 experiment [7, 8] and will be discussed in a future section.

1.4.1 Baryon Stopping

The measure by which something is measured is determined by the de Broglie wavelength of the probe,

$$\lambda = \frac{1}{p} \tag{1.5}$$

where λ is the wavelength of the probe and p is its momentum. In the case of heavy-ion experiments, both the probe and targets are the constituents of the incoming nuclei and their de Broglie wavelengths are determined by the momentum of the beam [33]. If the wavelengths are of the order of the size of the nucleons, as is the case for lower $\sqrt{s_{NN}}$ collisions, then the interaction scale is at the scale of nucleons, which are “imaged”. For cases like this, the interacting baryons encounter a “stopping” effect. Baryon stopping is defined as either the rapidity loss of projectile baryons or the rapidity gain of target baryons. If the momentum of an incoming baryon only has transverse momentum in the final state of the baryon, it is completely stopped. Baryon stopping describes the process by which the baryon number carried by incident nucleons is deposited into the resulting medium from the heavy-ion collision. When a large amount of incident baryon

number is deposited into the medium, the medium has a high μ_B and is baryon rich. As the $\sqrt{s_{NN}}$ of the heavy-ion collision increases, the de Broglie wavelength decreases and subsequently, the length scales also decrease. Therefore, the objects that are now starting to be imaged are the partons. The incoming baryons are transparent to each other as the length scale decreases to the scale of the partons. There is then less baryon stopping, and the μ_B values are lower.

The total baryon number is a conserved quantity and this means that any excess in baryon number (compared to anti-baryon number) is that which was deposited into the medium by stopping. New baryons created during the time evolution of the medium are balanced by the production of anti-baryons [33].

Chapter 2

STAR

2.1 Time Projection Chamber

The Time Projection Chamber is the main detector for tracking and particle identification (PID). In this section, a brief amount of detail about the TPC will be discussed. More information can be found in reference [3]. The shape is a large cylinder with a length of 420 cm and has an inner radius of 50 cm and outer radius 200 cm, as shown in Figure 2.1.

The z -axis is defined by the STAR magnet. The beam axis is tilted with respect to the z -axis (as defined by the magnet) by a few milliradians. Ideally, both would be the same, but they can only be as close as technology allows, and in the present case, there is a small but measurable difference between the beam axis and the axis of the magnet. The z -axis, running very close to parallel through the length of the pipe, ranges from $z = -210$ cm to $z = +210$ cm, with $z = 0$ cm at the center. The volume is filled with P10 gas (comprised of 90% Argon and 10% Methane) and is at a pressure slightly above atmospheric pressure such that if there is a leak, the outside air does not enter the volume. The argon, being the majority of the P10 gas, is an inert gas and as such, the ionization will only come from charged particles due to heavy-ion collisions. The presence of methane allows for some of the kinetic energy of the drifting electrons and ionized Argon atoms to be absorbed due to having many degrees of freedom and thus helps to maintain a constant drift velocity.

The TPC has two halves, divided by a central membrane kept at a negative voltage of magnitude 28 kV. Each end of the TPC is grounded and a uniform electric field of about

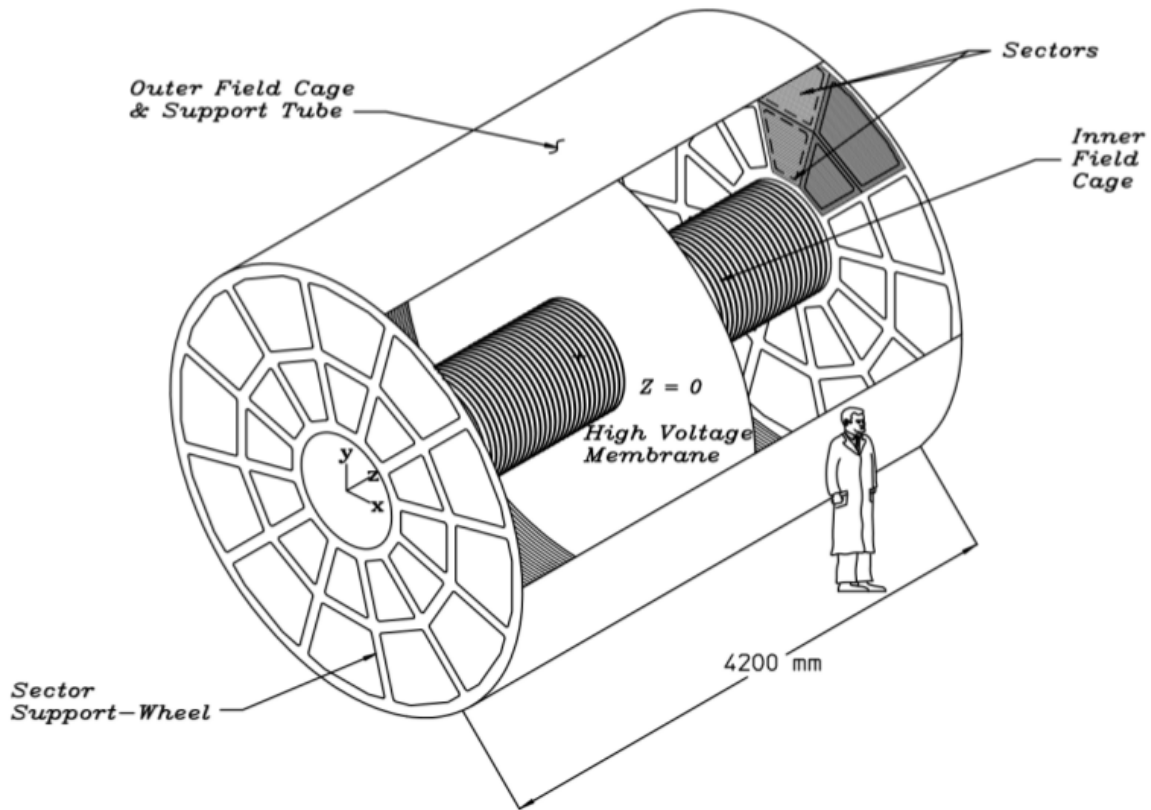


Figure 2.1: Schematic of STAR TPC (From [3])

133 V/cm is kept along the z -axis. During heavy-ion collisions, as charged particles pass through the TPC, the gas is ionized and the electrons drift outward, toward each end of the TPC and the positive ions drift toward the center of the TPC. The endcaps of the TPC are split into twelve sectors, each consisting of a gating grid, a multi-wire proportional chamber (MWPC), and pad planes, as shown in Figure 2.2. There are readout electronics on the back of the pad planes. The electrons drift toward the anodes, creating avalanches, amplifying their signal. The charge formed on the pad planes is then read out as a signal of the ionization energy lost by the initial charged particle that ionized the gas. From this information, the x and y coordinates of the ionization clusters are found. To find the z coordinate, more information is required. This coordinate can be found by using the drift velocity of the gas, the drift time it takes the clusters to reach the pad plane from the collision time, are needed to obtain the z coordinate. Every few hours during the run, lasers are turned on at known, fixed positions around the TPC and these are used to

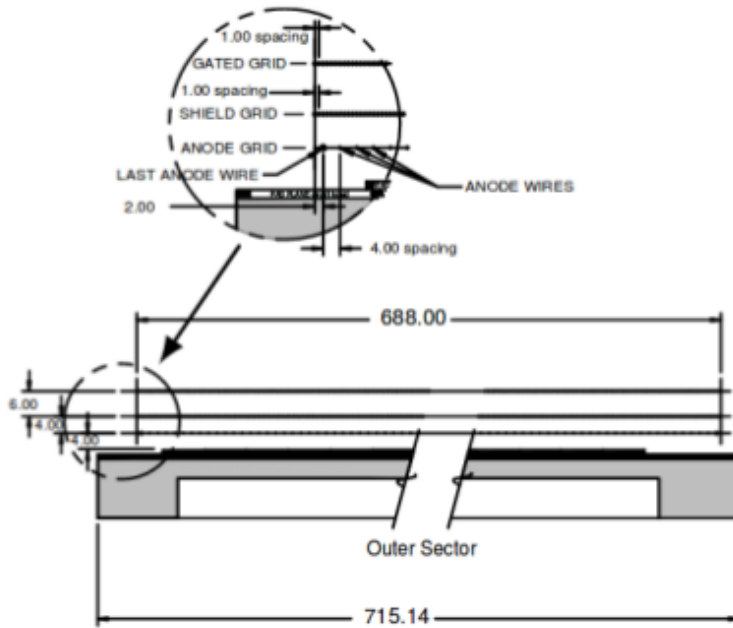


Figure 2.2: Diagram of the side view of one of the outer sectors. (From [3])

calibrate the drift velocity. Since the position and timing of the lasers are known, the drift velocity of the gas can be calculated. With this information, the z coordinate can now be found. The track reconstruction software then uses the 3-D space point measurements when fitting to obtain the track of the particles.

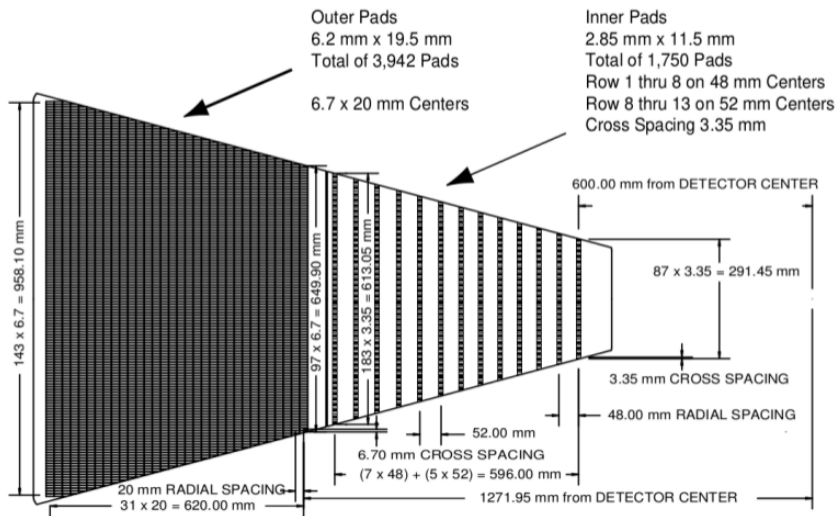


Figure 2.3: A schematic of a single anode sector of the TPC. The inner portion of the sector is on the right and the outer is on the left. (From [3])

In Figure 2.3, a diagram of one full pad plane is shown. There is an inner sector and an outer sector for each plane. There are 13 pad rows in the inner sector and 32 rows in the outer sector. This means the position and energy loss of a track can be recorded up to 45 times.

2.1.1 Particle Identification

The charged particles travel in a helical path in a magnetic field. For this reason, the track reconstruction algorithm fits a set of clusters (or hits) with helices creating global tracks. The vertexing algorithm then identifies possible collision vertices and the track reconstruction algorithm performs a refitting procedure to refit these global tracks with the inclusion of a vertex point. The vertex, having order of hundreds of tracks (or more) pointing to it, has a precision that is much better than the precision of any other point on a track, allowing for a much better determination of the track momentum. These resulting tracks are referred to as “primary tracks” as they now have a primary vertex.

In order to identify the particle, the measured momentum and energy loss are needed. To find the energy loss, the Bethe-Bloche equation is used as it relates the mean energy loss, $\langle dE/dx \rangle$, to the particle velocity, β .

$$-\left\langle \frac{dE}{dx} \right\rangle = \frac{4\pi}{m_e c^2} \cdot \frac{nq^2}{\beta^2} \cdot \left(\frac{e^2}{4\pi\epsilon_0} \right)^2 \cdot \left[\ln \left(\frac{2m_e c^2 \beta^2}{I \cdot (1 - \beta^2)} \right) - \beta^2 \right] \quad (2.1)$$

where m_e is the electron mass, c is the speed of light, $\beta = v/c$, q is the charge of the projectile particle, e is the charge of an electron, ϵ_0 is the permittivity of free space, I is the mean excitation and ionization potential of the material, and n is the electron density of the material. Here, n is defined as:

$$n = \frac{N_A Z \rho}{A M_u} \quad (2.2)$$

where N_A is Avogadro’s constant, Z is the atomic number of the material, ρ is the density of the material, A is the atomic mass of the material, and M_u is the molar mass constant. Figure 2.4 shows an example of the energy loss as a function of momentum over charge (where both dE/dx and momentum are measured). The bands correspond to different particles and charges.

PID with STAR TPC for $\sqrt{s_{NN}} = 4.9$ GeV Al + Au FXT Collisions

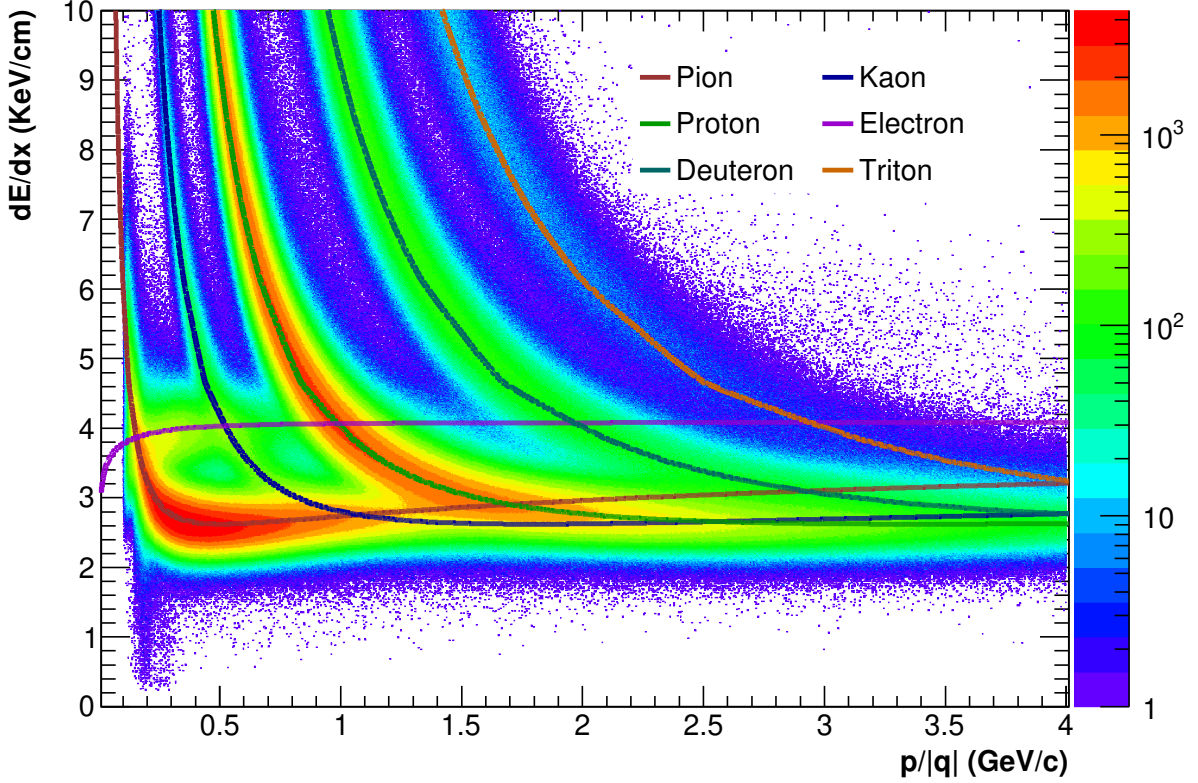


Figure 2.4: Energy loss (KeV/cm) as a function of momentum over charge (GeV/c) in the Time Projection Chamber. The bands correspond to different particles and charges.

However for describing the energy loss of tracks taken at STAR, a different method was used to find $\langle dE/dx \rangle$. A large amount of effort was done to understand the energy loss of particles in the P10 gas of the STAR TPC [34]; this resulted in the Bichsel Curves. Since there can be a maximum of 45 independent hits for a track in the TPC, there can then be up to 45 independent measurements of its dE/dx . The value of dE/dx at each hit is a Landau distributed random variable. The Landau distribution has a long tail toward higher dE/dx values. Therefore, if the mean dE/dx were used for up to 45 hits for describing the energy loss for each track, it can be skewed toward large values of dE/dx . To get around this issue, the largest 30% of measurements are not included for calculating the mean. The remaining 70% of measurements are used to calculate a truncated mean.

2.2 The Time of Flight

Like the TPC, the Time of Flight (TOF) detector is used for particle identification. However instead of energy loss, it is timing information that is used to identify particles. It is mounted outside the outer field cage of the TPC. In combination with the Vertex Position Detector (VPD), the TOF can be used to trigger on an event. The VPD are two identical scintillator detectors that are located symmetrically at $z = \pm 5.7$ m from the center of STAR [35]. The VPD is used to measure the start time of the collision and the TOF trays mounted outside the TPC measure the stop time of a given track. At the time of data collection, there are a total of 120 trays (60 on each side of the central membrane), azimuthally covering the TPC. In pseudorapidity, defined as:

$$\eta \equiv -\ln \left[\tan \left(\frac{\theta}{2} \right) \right] \quad (2.3)$$

where θ is the angle between the particle three-momentum and the positive direction of the beam axis, the covered range is $-1 < \eta < 1$. A single TOF tray contains 32 Multi-gap Resistive Plate Chamber (MRPC) modules. A diagram of a single module is shown in Figure 2.5 and a single TOF tray is shown in Figure 2.6.

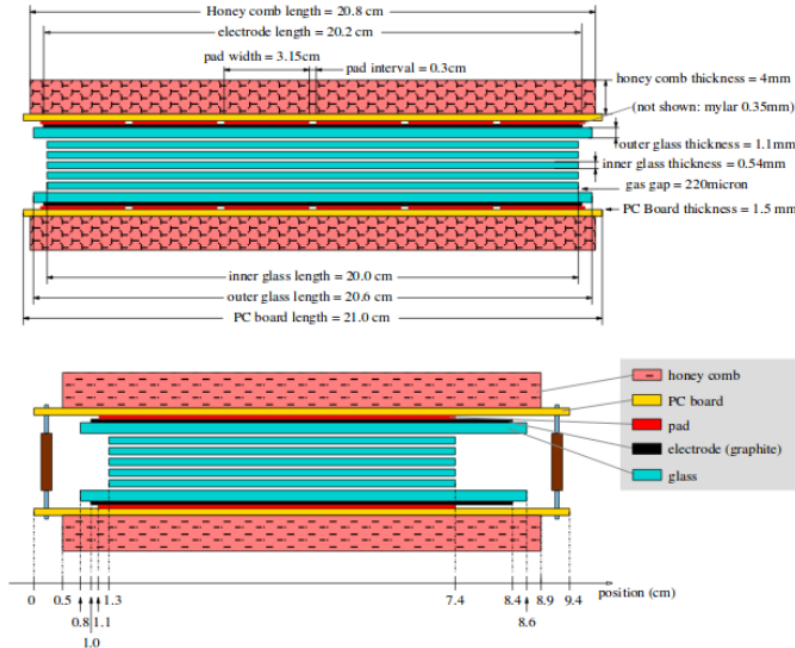


Figure 2.5: Side view of MRPC module (From [4])

This module is comprised of a stack of glass plates with gaps of freon gas in between. There is a high voltage (order 10 kV) applied across the outermost plates and, should a charged particle pass through a module, avalanches are generated across the gas gaps and the signal is the sum of all the generated avalanches. The resolution of the total time of flight is 100 ps.



Figure 2.6: Prototype design of schematic of a single TOF tray with projectively arranged MRPCs. (From [5])

The hits in the TOF pads are then matched to tracks in the TPC. Using the track

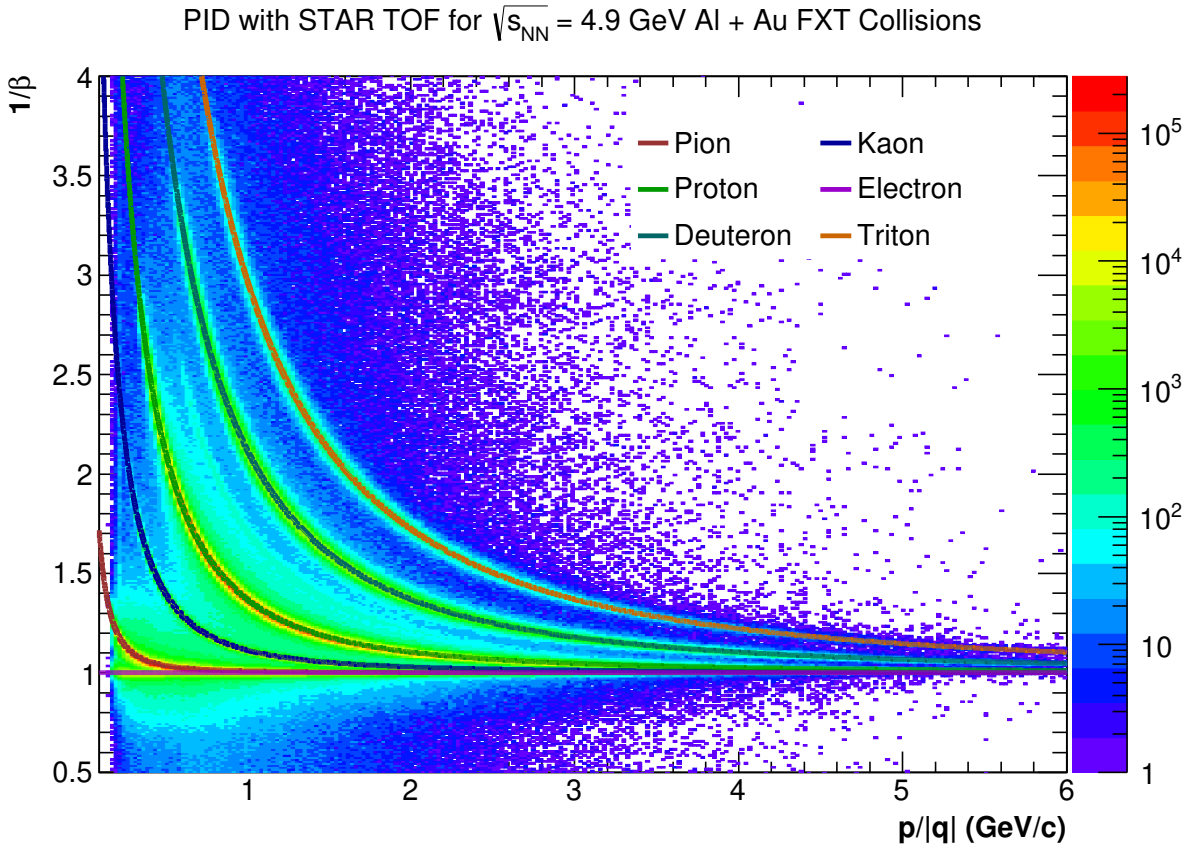


Figure 2.7: Inverse velocity as a function of momentum over charge (GeV/c) in the Time of Flight detector. The bands correspond to different particles of mass and charge.

path length, L , from information provided by the TPC and extrapolating to the TOF and the location of the primary vertex, as well as the the time of flight, the velocity of the particle can then be calculated.

$$\beta = \frac{L}{c\Delta t} \quad (2.4)$$

Since $E = \sqrt{p^2 + m^2}$ and $\beta = p/E$, the particle mass can be related to β through measured quantities.

$$m^2 = p^2 \left(\frac{1}{\beta^2} - 1 \right) \quad (2.5)$$

In Figure 2.7, the inverse velocity, $1/\beta$, is plotted as a function of momentum over charge. Each band corresponds to a different particle species.

2.3 Why study asymmetric systems like Al+Au?

In this context, a symmetric system means collisions of the same type of heavy ions. The first FXT dedicated test run, with a Au + Au system at $\sqrt{s_{NN}} = 4.5$ GeV, is an example of a symmetric system. Therefore, asymmetric systems are collisions involving different types of heavy ions. The Al + Au system at $\sqrt{s_{NN}} = 4.9$ GeV discussed in this body of work, is an example of an asymmetric system. An event display of this system is shown in Figure 2.8. Collisions of symmetric heavy ions do not create an isotropic equilibrated

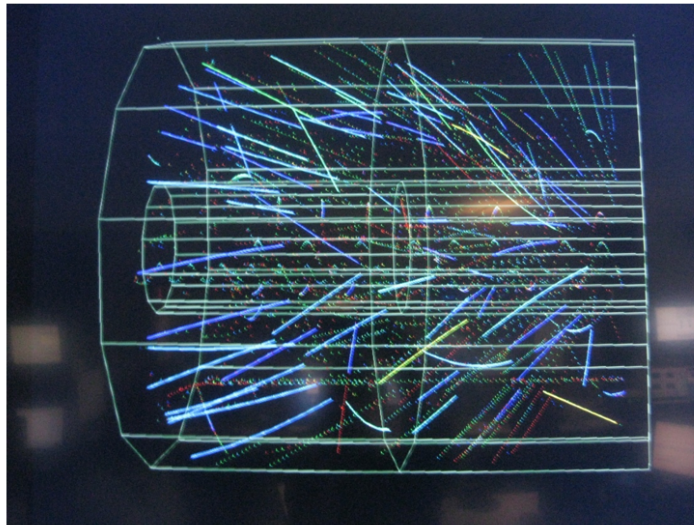


Figure 2.8: The event display for Al + Au collisions at $\sqrt{s_{NN}} = 4.9$ GeV.

static source. The interaction zone is characterized by gradients in pressure, chemical potential, temperature, and flow velocity. In asymmetric systems, varying thicknesses of

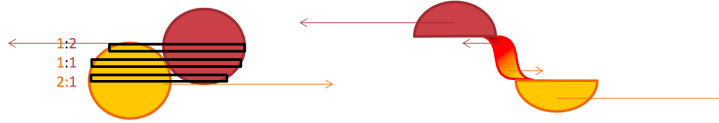


Figure 2.9: Asymmetric collision cartoon representing participants from both nucleons

nuclear matter from one participant overlap with varying opposing thicknesses. A cartoon of this is shown in Figure 2.9. The 4-5 GeV energy range is a regime of partial stopping. Baryon stopping is defined as either the rapidity loss of projectile baryons or the rapidity gain of target baryons. In collisions of symmetric nuclei, this partial stopping is seen as a broadening of the proton rapidity distribution. In asymmetric collisions, both the shift and the broadening of the rapidity distribution provide clues to the stopping. In central Al + Au collisions, the ratio of participants from the gold to aluminium nucleus is about 2:1. Thus Al + Au is a laboratory to study the upper and lower regions of rapidity and the interaction zone in semi-central Au + Au collisions.

Chapter 3

STAR Fixed-Target Al + Au 4.9 GeV Test Run

In 2015, two fixed-target test runs were conducted:

- The first test run was the run employed symmetric Au + Au collisions at $\sqrt{s_{NN}} = 4.5$ GeV, which used a single injected gold beam into the collider to, over time, skim the top edge of the 1 mm thick gold foil target. The probability of interaction from an incident beam ion is 4%. Former UC Davis nuclear physics graduate student, Kathryn Meehan, studied and analyzed this data set [36].

- The second test run was the asymmetric Al + Au at $\sqrt{s_{NN}} = 4.9$ GeV, which used a single injected aluminum beam into the collider to, much like the first test run, skim the top edge of the same 1 mm thick gold foil target. This body of work will be focusing on the second test run, Al + Au, but will reference the first test run.

3.1 Setup

The Au target was placed 1 cm outside the edge of the Time Projection Chamber (TPC) at $z = 211$ cm, ($z = 0$ cm is at the center of the TPC and the length of the TPC runs from $z = -210$ cm to $z = +210$ cm).

In collider mode, which has two beams colliding, the collision occurs around the center of the TPC allowing the full size of the TPC to be used for tracking. There is really a spread of locations and the width can be several or even tens of cm, depending on the

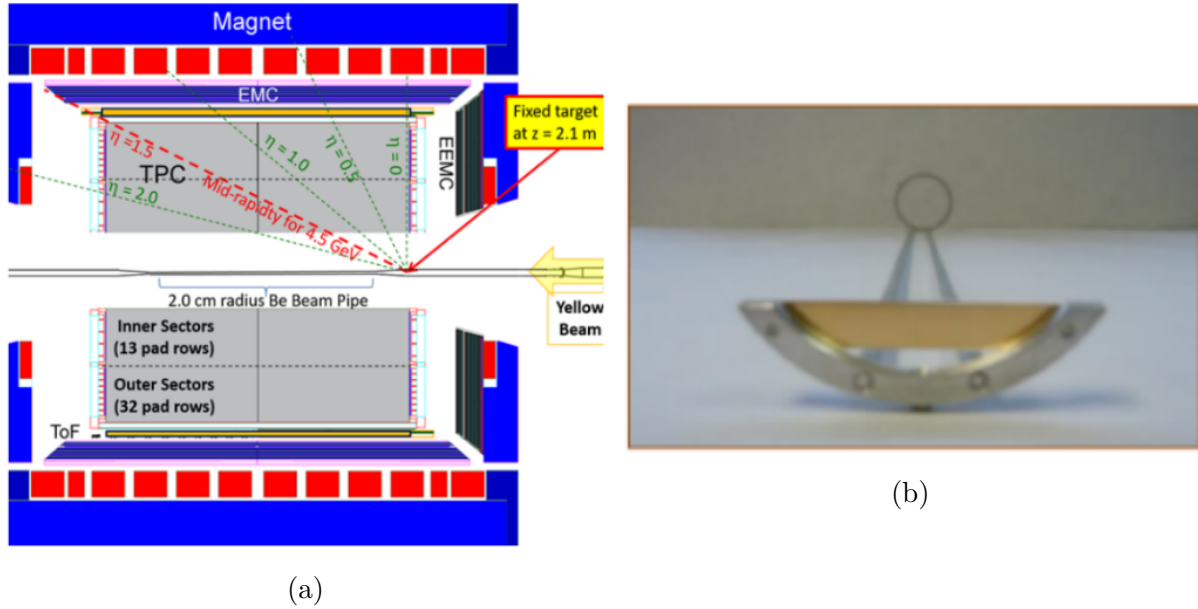


Figure 3.1: (a) A schematic of the 2015 Fixed-Target Au + Au test run. The incident Au beam enters the TPC from the West side (which is on the right side of this figure, the arrow pointing toward the fixed-target) and is eventually aimed to skim the top of the target, located 211 cm West of the center of the detector. (b) The gold foil target of height 1 cm, width 4 cm, and thickness 1 mm.

beams and energies involved. In order to allow for optimal tracking in the TPC in fixed-target mode, the target is placed on one edge of the TPC at $z = 211$ cm. The reason for this is because both the beam and the particles produced in the interaction will be traveling in same direction in z . This is shown in Figure 3.1. The incident Au beam enters from the West side of the TPC and is aimed to just graze the top of the Au target. The gold foil target has a height of 1 cm, a width of 4 cm, and a thickness of 1 mm.

3.2 Fixed-Target Trigger

To start collecting data, triggers are used. A trigger is a system that uses certain criteria to rapidly decide which events in a detector to collect. The criteria chosen for a trigger in the collection of this data is a hit in the Beam-Beam Counter (BBC) East Detector, a simultaneous veto in the BBC West detector, and a minimum Time-of-Flight (TOF) multiplicity. The BBC detectors are made of scintillator tiles that are used for triggering and for event plane measurements for analyses of flow[37, 38]. The reason why a veto on

the BBC West detector is part of the criteria is because the incident beam is traveling from the West side to the East side and so there should not be a hit in the BBC West detector. The TOF multiplicity is number of hits as measured by the TOF detector.

Table 3.1: The number of bunches, minimum TOF Multiplicity cut, number of triggers, number of vertices, and efficiency for each run number as well as the total for Al + Au runs at $\sqrt{s_{NN}} = 4.9$ GeV.

Run Number	# of bunches	TOF Mult Cut	# of Triggers	# of Vertices	Efficiency
16169070	1	40	526002	524580	99.73%
16169071	1	25	1000001	972144	97.21%
16169072	1	25	588368	571749	97.18%
16169074	2	40	590596	589144	99.75%
16169075	2	40	802377	800579	99.78%
Total			3507344	3458196	98.60%

Table 3.1 shows a summary of the run conditions. Runs 16169070-16169072 had only one bunch circulating and runs 16169074-16169075 had two bunches circulating. Run 16169073 was not included because it was a short run to make sure that the scale downs were correctly set. Different TOF multiplicity cuts were applied to see if there was an effect on the background.

This is the reason why the cut was lowered from a TOF multiplicity of 40 to 25 and then raised from a TOF multiplicity of 25 back to 40. The choice of these cuts can be seen in Figure 3.2 as vertical lines at values of 25 and 40 on the TOF multiplicity axis. The number of vertices refers to points that were reconstructed to be within 1 cm of the target, located between $210 \text{ cm} < z < 212 \text{ cm}$. In order for this to be a vertex, there must be at least two primary tracks that share this common location. The rate of background in this dataset was low, as shown by the efficiency column. It is also worth mentioning that the Au + Au runs had higher TOF multiplicity cuts (many runs had a cut of 130+). The reason for this is because of the background in the 2014 fixed-target test run of Au_{like} + Al collisions. There was a large background in the 2014 test run due to interactions with the Al beampipe. It was determined in the dedicated Au + Au fixed-

TOF Multiplicity

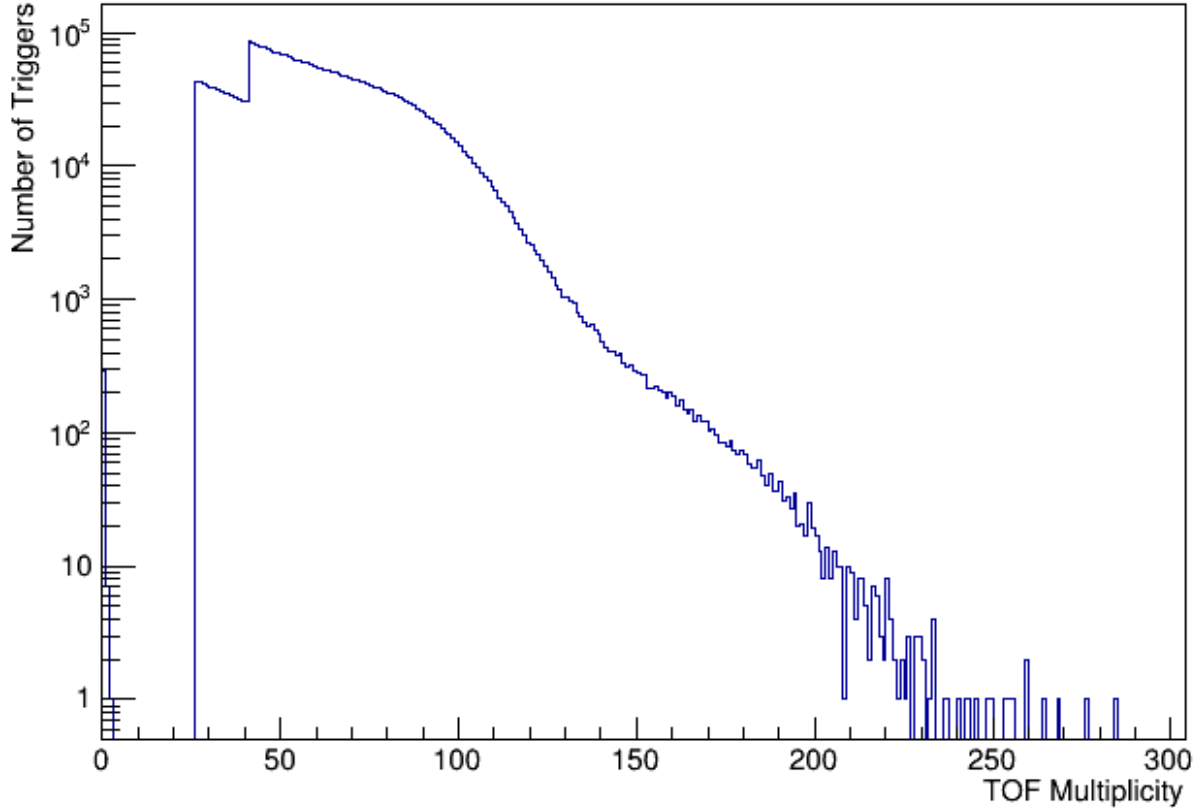


Figure 3.2: TOF multiplicity with event level cuts for Al + Au runs at $\sqrt{s_{NN}} = 4.9$ GeV. As can be seen in Table 3.1, the TOF multiplicity cut thresholds are visible at TOF multiplicity cuts of 25 and 40.

target run at $\sqrt{s_{NN}} = 4.5$ GeV that the TOF multiplicity cut could be lowered as the rate of background was relatively low [36].

In 2018, the fixed-target run had a minimum TOF multiplicity of 5. Gathering data in collider mode is limited by luminosity for statistics whereas in fixed-target mode, it is limited by the data acquisition (DAQ) rate. As luminosity is less of an issue for fixed-target mode (compared to collider mode), lower center-of-mass energies can be accessed by operating the collider in fixed-target mode.

3.3 Event, Vertex, and Track Selection

The applied cuts are across three different levels - event, vertex, and track cuts. The runs that had a FXT trigger ID were runs 16169070, 16169071, 16169072, 16169074, and

16169075, as mentioned in Table 3.1. Events that do not have at least one primary vertex are excluded. Vertex cuts involve only including primary vertices that are between 210 cm and 212 cm as the gold target is fixed at $z = 211$ cm. By applying this cut, a large fraction of the background is removed.

Selection Criteria:

- Trigger ID == 1
- $210 \text{ cm} < |V_z| < 212 \text{ cm}$

For these runs, the FXT trigger ID that satisfies the conditions as described in section 3.2 is Trigger ID == 1. This selection criteria is used to make cuts on the data for analysis. We employ only a 1D geometric vertex (the z -position, no requirements on the x or y positions of the vertex) requirement and we require that the primary vertex be the index 0 vertex identified by the vertex algorithm. This cut is only necessary if the time-of-flight information is being used. A typical event (or trigger) has multiple vertices which are sorted by the vertex ranking algorithm [39]. Index 0 vertices are likely correspond to the vertices of the most interesting collision in the event. It should also be mentioned that the vertex ranking algorithm was not optimized for the fixed-target configuration at the time. Not all vertices that are within range of the selection criteria of the target were 0 index vertices.

The first cut is sufficient to localize interactions to within the gold target. Figures 3.3a and 3.3b show the V_z and $V_x - V_y$ distributions of all vertices prior to event cuts, while Figures 3.4a and 3.4b shows the distributions after the event cuts. The tails of the V_z distribution are sharply truncated at the cut locations and the haze around the core of the $V_x - V_y$ is significantly reduced indicating that most of these off-axis vertices are offset in V_z . As it is clear that no Al + Au collisions occur outside of the target, this figure best illustrates the resolution of the vertex reconstruction. From Table 3.1, it should be noted that 98.6% of events had a primary vertex within the target.

The requirement that only the index 0 vertices were used is necessary to ensure that the TOF information is correct. To determine the start time of the collision, the TOF usually

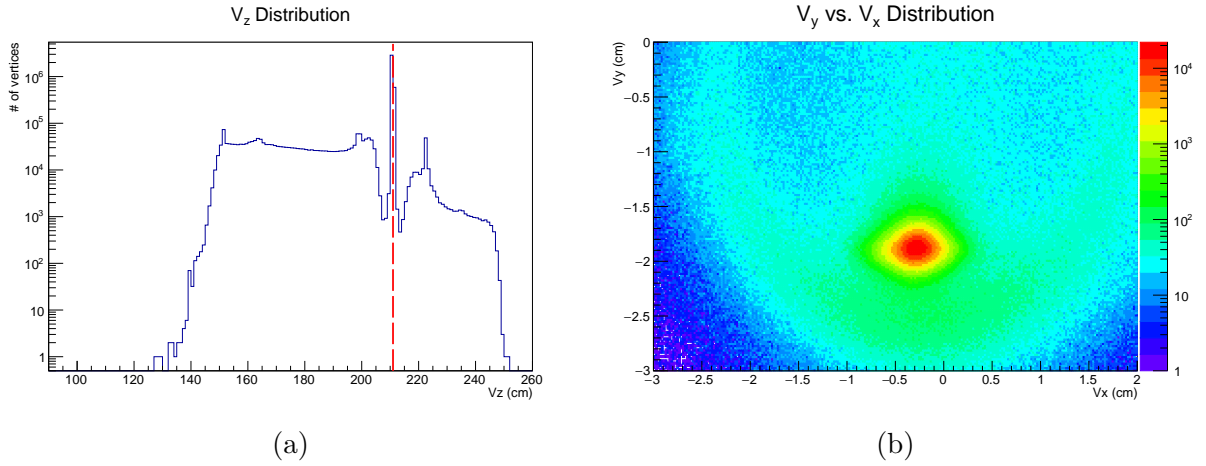


Figure 3.3: (a) The full set of reconstructed vertices. The Au target is located at $V_z = 211$ cm, as shown by the vertical dashed line. (b) The $V_x - V_y$ distribution of reconstructed vertices in the vicinity of the target prior to event selection cuts.

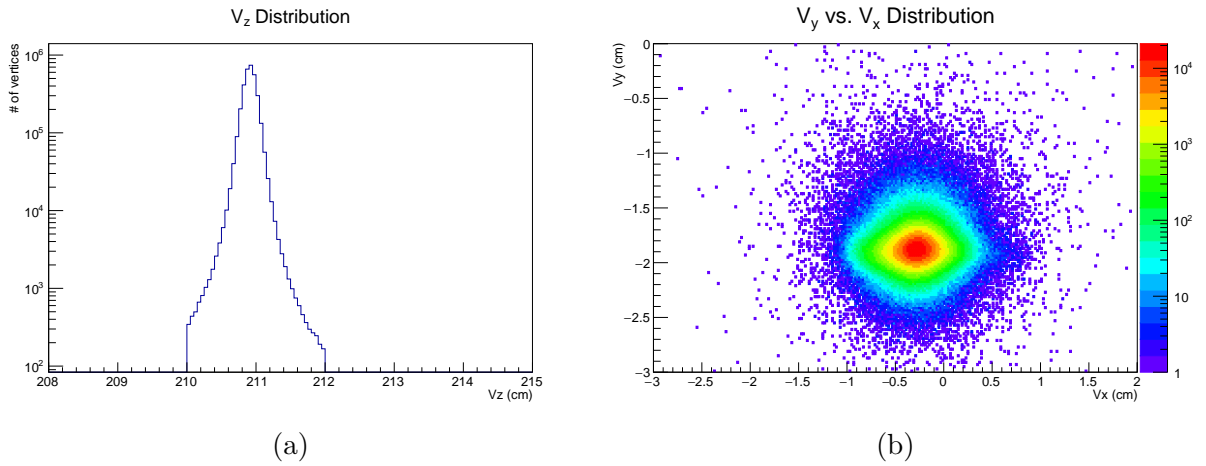


Figure 3.4: (a) The V_z distribution of reconstructed vertices after event selection cuts. The Au target is located at $V_z = 211$ cm. (b) The $V_x - V_y$ distribution of reconstructed vertices after event selection cuts.

relies on the VPD. However, in a FXT configuration (one single beam), a VPD coincidence is not possible and the TOF uses the communal start algorithm to reconstruct the time-of-flight information of the individual TOF time to digital converter (TDC) signals. This algorithm selects the index 0 vertex to determine the trigger start time, therefore the TOF information for all other vertex indices is incorrect. At this time, events had on average 1-2 primary vertices identified by the vertex algorithm. Many of these come from secondary interactions with the beam pipe. Another source of spurious vertices is out-of-time interactions with the target. Both sources of non-primary vertices can be seen in Figure 3.3a. The out-of-time collisions are seen as the spikes that are offset in multiples of ± 11 cm from the target location. These spikes are offset by ± 11 cm because there were only two buckets filled in the yellow ring; each filled bucket is offset by $2 \mu\text{s}$. Since the TPC drift speed is $5.5 \text{ cm}/\mu\text{s}$, the out-of-time vertices are offset in multiples of 11 cm. The secondary interactions with the beampipe are seen in Figure 3.3a as the relatively constant plateau between 150 and 200 cm. Note that the vertex finder software was set to only search for vertices in the range from 150 to 250 cm. The vertexing software also selects which vertex to identify as the primary vertex. Sometimes the software erroneously identified an out-of-time vertex as the primary vertex even though there is the correct vertex found within the target. The requirement that we use only primary vertices reduces the trigger efficiency to 95.5%, which is still quite high.

The track cuts mentioned below are made when producing the official MuDsts. The primary tracks in the official MuDsts have the following cuts:

- $\text{nHitsdEdx} > 5$
- $\text{nHitsFitTPC} > 10$
- $\text{nHitsFit}, \text{nHitsPoss} > 11$
- $\text{gDCA} \leq 3$

The number of dE/dx hits that a track has is nHitsdEdx . The number of hits in the TPC is that could be associated for a given track is nHitsFitTPC . The number of hits in the TPC plus the primary vertex counted as a hit is nHitsFit . The global distance of

closest approach (**gDCA**) is the magnitude of distance between the primary vertex and the closest point on the reconstructed global track that passes the primary vertex. There are tracks with **gDCA** > 3 , but the number of these tracks is about three orders of magnitude fewer. One more requirement is that the ratio of **nHitsFit** to the number of hits that could have been used, **nHitsPoss**, be greater than 0.52 or equal. The reason for this is to eliminate short tracks that may have been sections of one track but were reconstructed by the tracking algorithm as two separate tracks. An important thing to mention is that in the fixed-target configuration, many of the tracks will cross the central membrane of the TPC, and many of the split tracks are due to this.

Chapter 4

Centrality Selection

The interaction zone of two colliding nuclei will depend on the overlap region of the two nuclei. Properties of the interaction zone, such as its size, will depend on the collision species as well as the impact parameter, b . As the impact parameter is not directly measurable, the centrality of an event can be determined through particle multiplicity as smaller impact parameters will coincide with an increase in particle multiplicity.

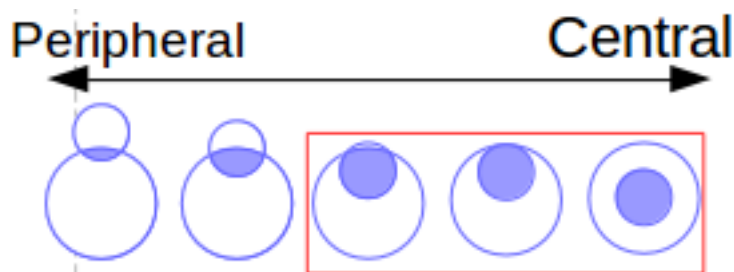


Figure 4.1: A cartoon showing the overlap region for a collision between an aluminum nucleus and a gold nucleus at different centralities. For more central collisions, the aluminum nucleus is engulfed by the gold nucleus.

In doing this, the centrality of events can be binned using particle multiplicity. Through Monte-Carlo simulations of nucleus + nucleus collisions, distributions for the impact parameter, number of participants, N_{part} , and number of binary collisions, N_{coll} , can be created. The impact parameter is the perpendicular distance between the path of the center of a projectile nucleus relative to the center of another nucleus that the projectile nucleus is approaching. Figure 4.1 shows a cartoon of the overlap region (shaded) between an aluminum nucleus and a gold nucleus at varying centralities ranging from cen-

tral (where the centers line up with no impact parameter) to more peripheral centralities (non-zero impact parameter). The number of participants is a quantity that describes the sum number of nucleons participating in a collision from each parent nucleus. The number of binary collisions is a count of the number of individual collisions between a projectile nucleon and a target nucleon.

The centrality of the Al + Au collision is determined by comparing the results of a Glauber Monte-Carlo model to the event-by-event charged particle multiplicity, as shown in Figure 4.2 [40]. In the Glauber model, nucleons are randomly distributed according to a Woods-Saxon function for each nucleus. An impact parameter is randomly chosen and the transverse position of each of the nucleons is computed. The relative transverse distance between all pairs of nucleons (one from the target nucleus and one from the projectile) is calculated. If this distance is less than $2\sqrt{\sigma_{pp}/\pi}$, where σ_{pp} is the inelastic proton-proton cross-section, for $\sqrt{s_{NN}} = 4.9$ GeV collisions is found from the particle data book to be 30 mb, each nucleon is identified as a participating nucleon and the pair is counted as having had a binary collision. All participating nucleons and binary collisions are summed to determine N_{part} and N_{coll} .

Charged particle production is modeled with the Negative Binomial (NB) distribution,

$$\text{NB}(n_{pp}; \langle n_{pp} \rangle, k) = \binom{n_{pp} + k - 1}{k - 1} \left[\frac{\langle n_{pp} \rangle / k}{1 + \langle n_{pp} \rangle / k} \right]^{n_{pp}} \frac{1}{[1 + \langle n_{pp} \rangle / k]^k} \quad (4.1)$$

where $\langle n_{pp} \rangle$ is the average multiplicity of a $p + p$ collision at the energy of interest and the parameter k is related to the variance of the $p + p$ distribution [33]. For each Al + Au collision the NB is sampled N_{part} number of times. The parameters n_{pp} and k of the $\text{NB}(n_{pp}; \langle n_{pp} \rangle, k)$ are determined using a grid search method — looping through various combinations of the parameters and performing a χ^2 test each time until an acceptable χ^2 was found. The χ^2 describes how the closely the observed data matches that of the expected value or result from a model. The particle multiplicities for many Al + Au Glauber Monte-Carlo collisions were aggregated and the particle multiplicity distribution was integrated to find the multiplicity corresponding to a given percentage of the total inelastic cross section.

Figure 4.2 shows the results of the Glauber model compared to the measured multi-

plicity distribution. It is clear that the data set does not match the Glauber Monte Carlo for either low or high multiplicities. For low multiplicity events, the data fall well below the Monte Carlo because we did not attempt to employ a minimum bias trigger. The trigger was intended to select effectively the top 30% most central events. The motivation for running only a central trigger was the concern that a minimum bias trigger would be swamped by low multiplicity background coming from beam halo interactions with material. This did not turn out to be the case and we could probably have safely reduced the TOF multiplicity selection requirement significantly. This would have allowed accumulation of more peripheral events. As it is, there are some peripheral events recorded, however these will be biased by the TOF multiplicity trigger bias. The trigger shows little bias for central events. The data also do not match the Monte Carlo for multiplicities above 125. The events with multiplicities greater than 125 come from multiple interactions within the target during a single bunch crossing. These pile-up events have been studied, and we have determined that they make up less than 0.8% of all triggers. This can be reduced for a dedicated physics run by using a thinner target and filling more buckets. The cuts for various centralities and to eliminate pile-up are indicated in Figure 4.2.

The trigger efficiencies for the 0-5%, 5-10%, 10-15%, 15-20%, 20-25%, and 25-30% centrality classes are 97%, 96%, 99%, 97%, 92%, and 95% respectively. The pile-up was modeled with a Monte-Carlo simulation. To create the simulated multiplicity distribution with pile-up, we filled a histogram with events with a multiplicity obtained by randomly sampling the data distribution up to a multiplicity of 125. Beyond this multiplicity we expect the vast majority of events to be pile-up events. Additionally for an assumed, small percentage of events, the “minimum bias” Glauber Monte-Carlo + Negative Binomial fit to the data was sampled and the multiplicity of that was added to the multiplicity of the first event sampled from the data distribution. A minimum-bias distribution was used for the other collision of the pile-up event since only the combined multiplicity of the two events had to be sufficient to satisfy the trigger conditions. The resulting distribution was then fit to the originally measured distribution. This procedure was

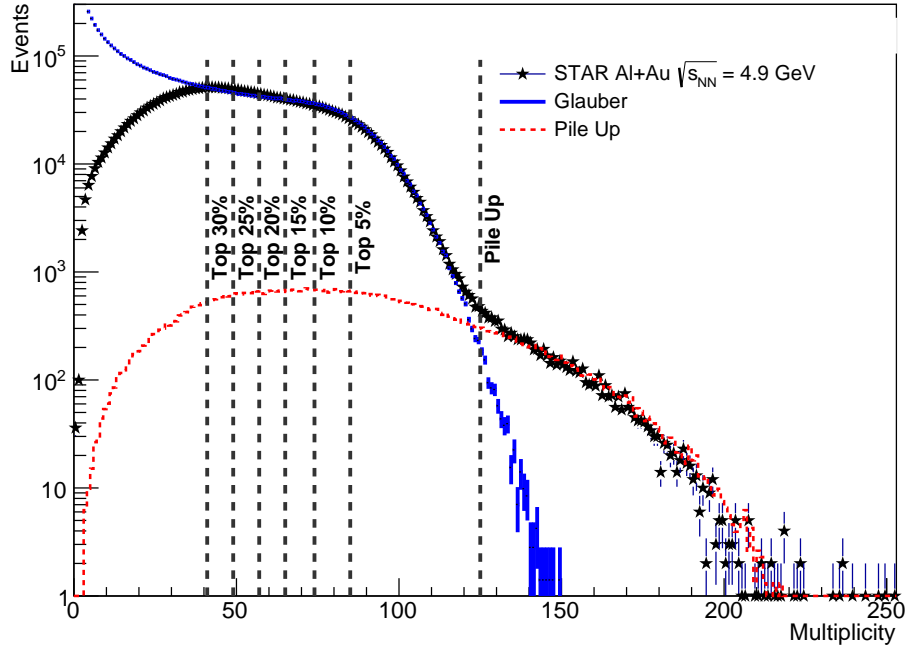


Figure 4.2: The centrality selection for the STAR FXT Al + Au collisions at $\sqrt{s_{NN}} = 4.9$ GeV. The centrality variable depends on the number of tracks that pass track quality assurance cuts. The distribution of events with a given multiplicity of good tracks is shown with solid black circles. The blue curve is the Glauber Monte-Carlo + Negative Binomial fit to the data. The red dashed curve is a Monte-Carlo model of pile-up events. The black dashed lines show the centrality selection lines for top 30%, 25%, 20%, 15 %, 10%, and 5%. In addition, a dashed black line is shown at a multiplicity of 125, which illustrates the high multiplicity pile-up cut; events with greater than this multiplicity were most likely to have resulted from two Al + Au collisions within the target during the same beam bunch and were excluded from this analysis.

repeated assuming different percentage values for the fraction of events that were pile-up, and a chi-squared minimization was done in the pile-up dominated region to optimize this percentage, which was estimated to be 0.8%. The red curve in Figure 4.2 is the resulting simulated distribution of just the pile-up events. Events with a multiplicity greater than 125 have been excluded from this analysis as this region of multiplicity is dominated by pile-up events.

The estimate of the percentage of events that are pile-up events for each centrality bin is given in Table 4.1. An upper limit on the multiplicity for an event in the top 5% centrality bin was chosen to be 125. A stricter cut could be used for analyses more

sensitive to pile-up such as moments analyses.

Table 4.1: The centrality bins used in the analyses. Included are the average number of participating nucleons (N_{part}) for each centrality class, as well as the break down of how many of those nucleons were contributed by the aluminum projectile and how many were contributed by the gold target as calculated using a Glauber Monte Carlo model. Each bin corresponds to 5% of the total cross section.

Centrality(%)	N_{Events}	$\langle N_{\text{part}} \rangle$	$\langle N_{\text{part}}^{\text{Al}} \rangle$	$\langle N_{\text{part}}^{\text{Au}} \rangle$
0 - 5	331206	100 ± 2	26.5	73.8
5 - 10	338478	89 ± 4	25.9	63.4
10 - 15	337787	80 ± 3	24.9	55.1
15 - 20	338305	70 ± 3	23.4	46.8
20 - 25	376610	62 ± 2	21.6	39.6
25 - 30	404982	53 ± 2	19.6	33.5

Chapter 5

Extracting the Raw Yields

To obtain the spectra for a particle species, the data is then further divided into multiple rapidity and $m_T - m_0$ bins. m_T is the transverse mass, which is defined as $m_T = \sqrt{p_T^2 + m_0^2}$ (where p_T is the transverse momentum), and m_0 is the rest mass of the particle. The reason for dividing the bins into $m_T - m_0$, as opposed to perhaps p_T , is because the fitting function that will be used will appear linear when plotted in a semi-log scale. In order to get the raw spectra, the raw yields are first obtained in each of the centrality, rapidity, and $m_T - m_0$ bins by using a multiple Gaussian fit to z_{TPC} distributions. The z_{TPC} variable is defined by

$$z_{\text{TPC}} = \log \left(\frac{dE/dx_{\text{meas}}}{dE/dx_{\text{exp}}} \right) \quad (5.1)$$

where dE/dx_{meas} is the energy loss measured in the TPC and the dE/dx_{exp} are the expected values from the Bichsel curves.

For the π^- , the particles that could potentially contaminate the z_{TPC} distributions are the e^- , the K^- , and the antiprotons. There are so few antiprotons due to the low $\sqrt{s_{NN}}$ of this dataset, that their contribution has been ignored. As for the K^- , though they start to overlap with the π^- at lower momentum values than the antiprotons, they too are still outside of the $m_T - m_0$ range of this work and have not been considered in the fitting procedure. A multiple Gaussian fit is performed over the pions and electrons to extract the raw yield for the π^- . A multi-round fit procedure was done to reduce the number of free parameters. In the first round, a single Gaussian was applied to the π^- with the goal

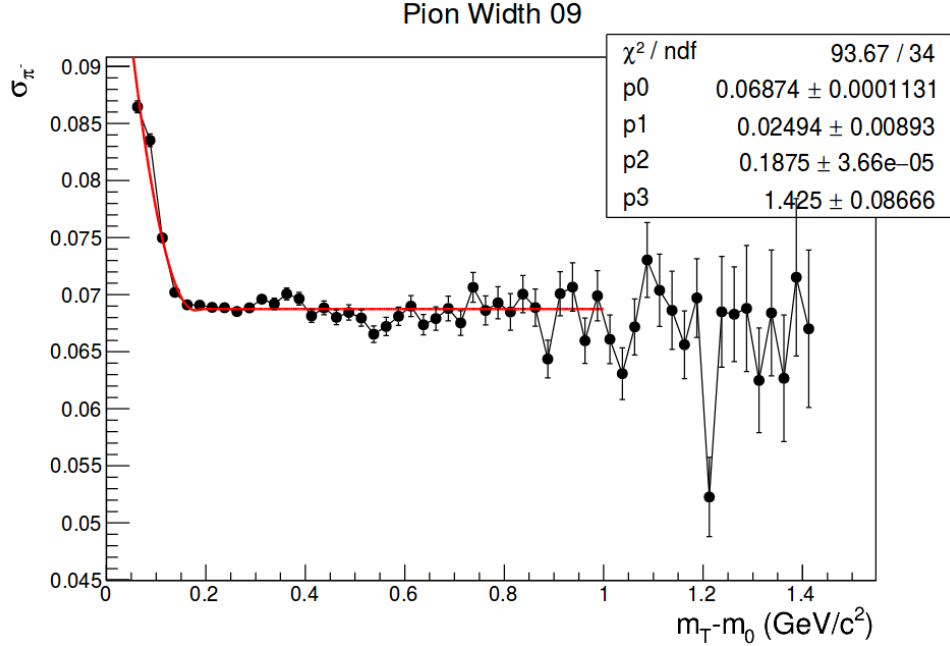


Figure 5.1: Fixing of the pion width parameter in double Gaussian fit for pion yield. This is done for each centrality, rapidity, and $m_T - m_0$. This fit is a piecewise polynomial.

of parameterizing the pion width. An example of this multi-round fit procedure is shown later in this chapter.

The pion width is fit with a piecewise function of a constant and a polynomial. and is described in Equation 5.2. A polynomial is used because there is no physical motivation for the transverse mass dependence; this is an indication of imperfect TPC calibrations. The calibrations are done by assuming all tracks are pions. Therefore, if the calibrations were perfect, the pion mean should be zero and the width should be the resolution of the TPC. This fit was performed in Figures 5.1 and 5.2.

$$f(m_T - m_0) = \begin{cases} p0 + p1((m_T - m_0) - p2) + p3((m_T - m_0) - p2)^2 & m_T - m_0 \leq p2 \\ p0 & m_T - m_0 \geq p2 \end{cases} \quad (5.2)$$

The widths are then plotted as a function of $m_T - m_0$ for this given centrality and rapidity bin and fit with a polynomial function, and for subsequent rounds, fixed at the evaluated fit function value for a given $m_T - m_0$ bin. In the second round, the pion mean from the Gaussian fit is fixed at zero and a double Gaussian is used to fit both the π^- and e^-

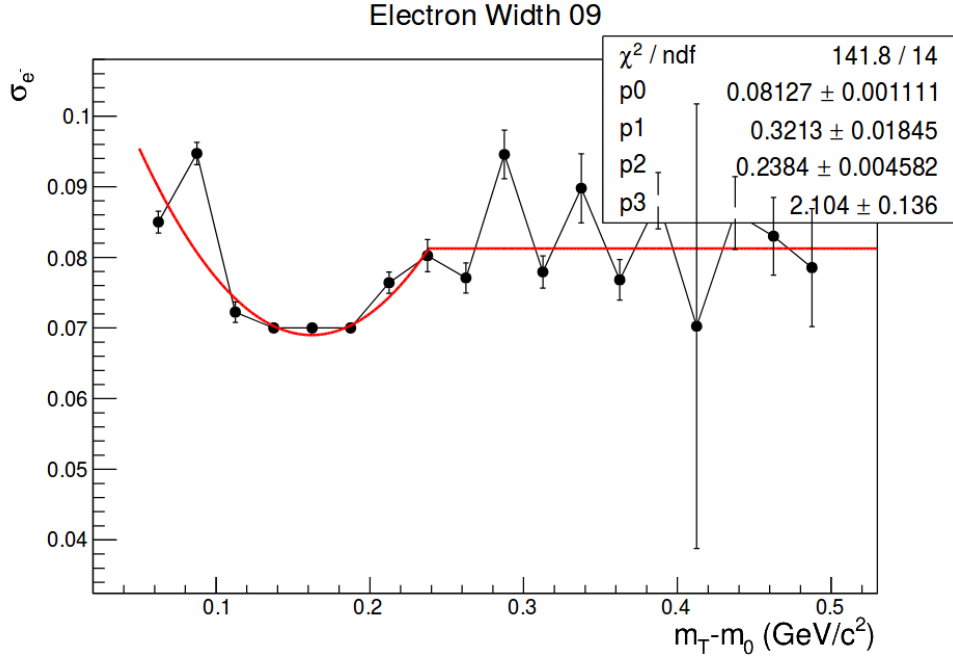


Figure 5.2: Fixing of the electron width parameter in double Gaussian fit for pion yield. This is done for each centrality, rapidity, and $m_T - m_0$. This fit is a piecewise polynomial.

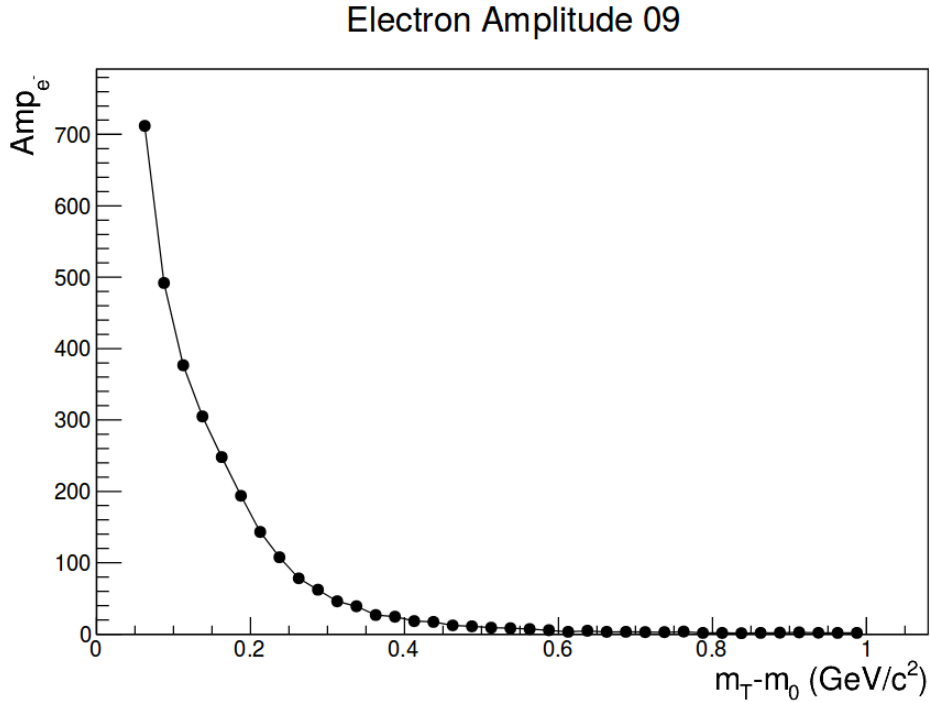


Figure 5.3: Fixing of the electron amplitude parameter in double Gaussian fit for pion yield. This is done for each centrality, rapidity, and $m_T - m_0$. The values at each bin are used.

peaks. The electron means and widths are then plotted as a function of $m_T - m_0$ for the same centrality and rapidity bin, fit with a fitting function, and then fixed for the next round. In the third round, the double Gaussian fit is repeated with now only the two amplitude parameters free. For the final round of fitting, the electron amplitude values are not fit with any function, as shown in Figure 5.3, and instead the values from the third round are used. In this fit, only the pion amplitude is free.

The raw yield can be then be calculated from integrating the Gaussian fit function,

$$\frac{1}{2\pi m_T} \frac{d^2 N}{dm_T dy} = N \left(\sqrt{2\pi} A \sigma \right) \quad (5.3)$$

and with normalization,

$$N = \frac{1}{2\pi m_T} \frac{1}{N_{\text{Events}} \Delta z_{\text{TPC}} \Delta y \Delta (m_T - m_0)} \frac{d^2 N}{dm_T dy} \quad (5.4)$$

where the $(\sqrt{2\pi} A \sigma)$ term comes from the integration of the Gaussian. The $1/(2\pi m_T)$ is included for a Lorentz invariant yield.

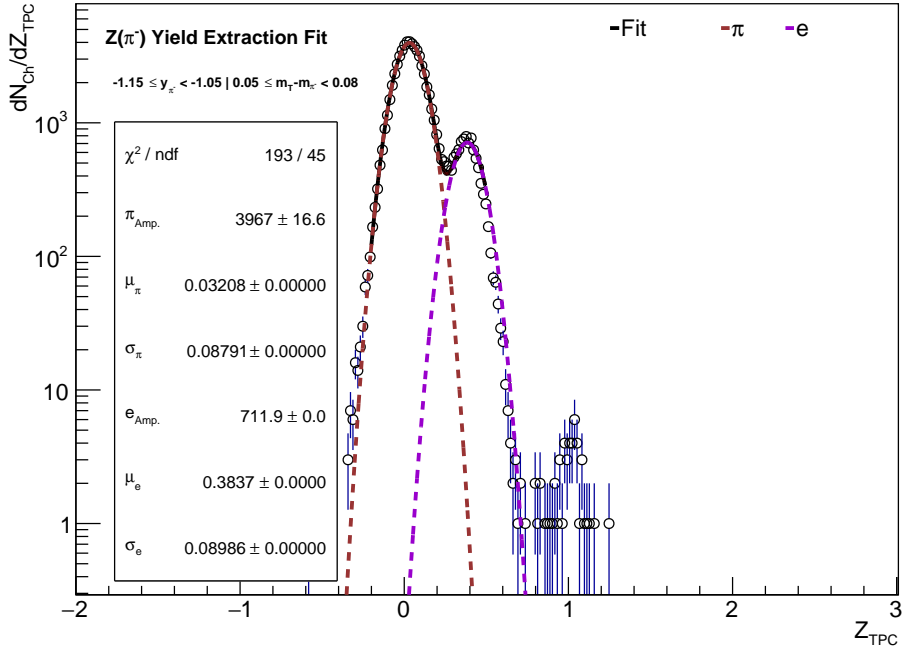


Figure 5.4: The z_{TPC} fit of the pions (brown dashes) and electrons (purple dashes) for the 0-5% centrality bin, beam rapidity $y = -1.1$, and $m_T - m_0 = 65$ MeV bin.

The N_{Events} are the number of events in a given centrality bin (see Table 4.1). The bin width of the z_{TPC} plots, Δz_{TPC} , is 0.015. The rapidity bin width is Δy and the transverse

mass bin width is $\Delta(m_T - m_0)$. The rapidities are binned in slices of width 0.1 and the $m_T - m_0$ bins have a 25 MeV width. The lab rapidities included for the π^- are from $y_{\text{lab}} = -0.2$ to $y_{\text{lab}} = -1.8$. An example of the π^- yield after the multiple rounds of fitting is shown in Figure 5.4, at beam rapidity slice $y = -1.1$ and the transverse mass bin of $m_T - m_0 = 65$ MeV.

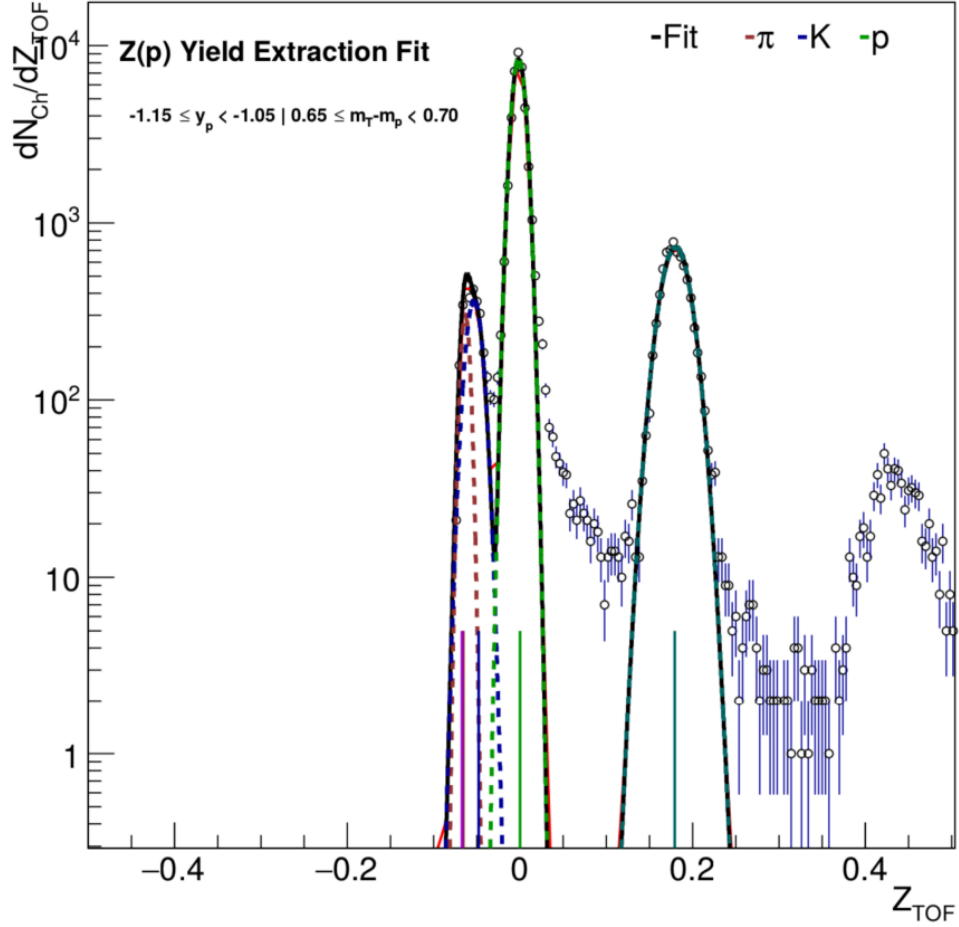


Figure 5.5: The z_{TOF} fit of the protons (green dashes), pions (brown dashes), kaons (blue dashes), and deuterons (blue-green dashes) for the 0-5% centrality bin, beam rapidity $y = -1.1$, and $m_T - m_0 = 65$ MeV bin. Plot created by Sam Heppelmann.

Fellow UC Davis graduate student Sam Heppelmann worked on the proton analysis for this dataset and has performed a similar, but modified, method for obtaining the raw proton yields. Figures 5.5 and 5.6 were created by Sam. The lab rapidities range from 0.2 to 1.3 and the transverse mass bins are divided into widths of 50 MeV. As the protons are more contaminated by contributions from other species, the proton z_{TPC} distributions are

histogrammed with a matching Time of Flight (TOF) requirement. The z_{TOF} variable, defined in Equation 5.5, was used to make a clean proton z_{TPC} distribution; this was done by applying a 2σ cut in the z_{TOF} fits.

$$z_{\text{TOF}} = 1/\beta_{\text{meas}} - 1/\beta_{\text{exp}} \quad (5.5)$$

To fit a clean z_{TPC} distribution, the width is used in the original z_{TPC} distribution as a fixed parameter. The z_{TPC} of tracks identified as a proton in the TOF are fit with a single Gaussian and their widths and means are parameterized in the matched z_{TPC} histograms. Due to the lower efficiency in the TOF, the means and widths from the matched z_{TPC} histograms are applied to the unmatched z_{TPC} histograms and the amplitude parameter was permitted to float. As there are no antiprotons, this helps to set the parameters of the π^+ and e^+ , which contaminate the proton distributions. A fourth Gaussian is included for the deuterons and the same technique as the protons is applied to find the means and widths of the deuterons in a TOF matched z_{TPC} signal.

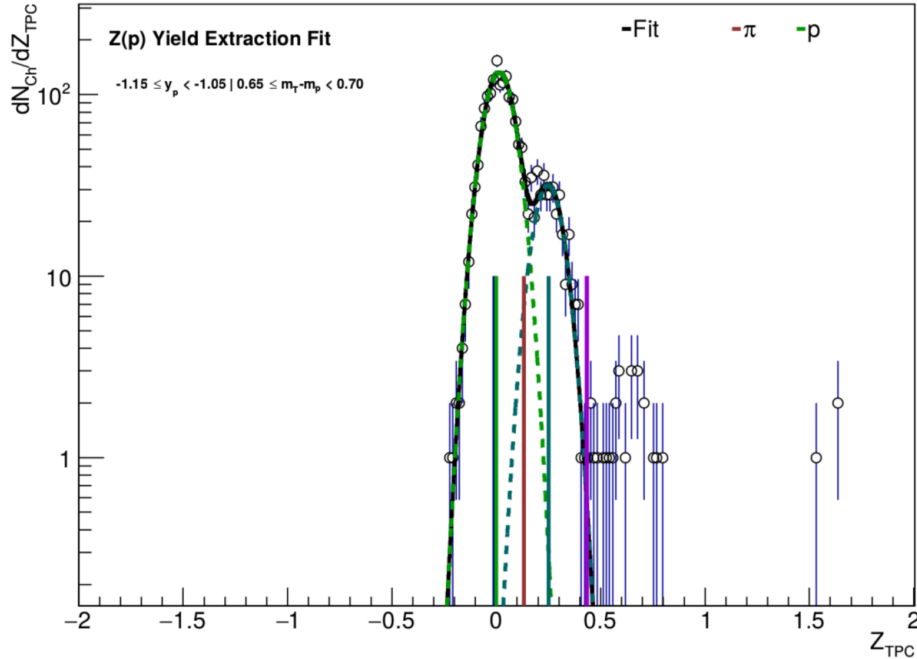


Figure 5.6: The z_{TPC} fit of the protons (green dashes) and pions (brown dashes) for the 0-5% centrality bin, beam rapidity $y = -1.1$, and $m_T - m_0 = 65$ MeV bin. Plot created by Sam Heppelmann.

Chapter 6

Efficiency Corrections

As the STAR detector does not have perfect efficiency that fall within its acceptance, efficiency corrections need to be applied. The acceptance issues are most noticeable at low transverse masses. The reason for this is because of the implicit `nHitsFit` cut in the STAR track reconstruction software that requires a minimum of 10 hits in the TPC. At low $m_T - m_0$, tracks can exit the detector without traveling sufficiently outward in the radial direction to have hits in at least 10 pad rows. Furthermore, in this Fixed-Target geometry, with the target at location $z = 211$ cm, outside the volume of the TPC, there will be tracks that have low, close to zero, rapidity and high $m_T - m_0$; many of these tracks will not leave hits in at least 10 pad rows.

Efficiency corrections are done by embedding Monte Carlo tracks into real data and then running them through GEANT [41] – a software framework which can be used to model the STAR detector and then simulate its response to tracks passing through. This process is known as “embedding” as it involves embedding Monte Carlo generated tracks into real data. The data is then reconstructed using the GEANT detector model of STAR and the full STAR reconstruction software. To distinguish the tracks, there are embedded tracks, reconstructed tracks, and matched tracks. An embedded track is a track that originated from the Monte Carlo model where everything about the track is known such as its kinematic properties and position. A reconstructed track is one that has been reconstructed by the reconstruction software. Lastly, a matched track is also a reconstructed track that is able to be matched back to one of the Monte Carlo embedded

tracks. This process is done for each species of particle covering all centrality bins and embedded rapidity bins. The efficiency as a function of embedded $m_T - m_0$ is defined as,

$$\epsilon(x) = ae^{-b/x^c} \quad (6.1)$$

where, for a given centrality and rapidity bin, ϵ is the tracking efficiency, x is the embedded $m_T - m_0$, and a (the value at which the function will flatten), b (how sharply the function flattens), and c (affects where in x the function begins to rise) are the fit parameters. For the π^- and protons that are not in in regions of acceptance issues, the efficiency plateaus at just over 80%. An example of Equation 6.1 is shown in Figure 6.1.

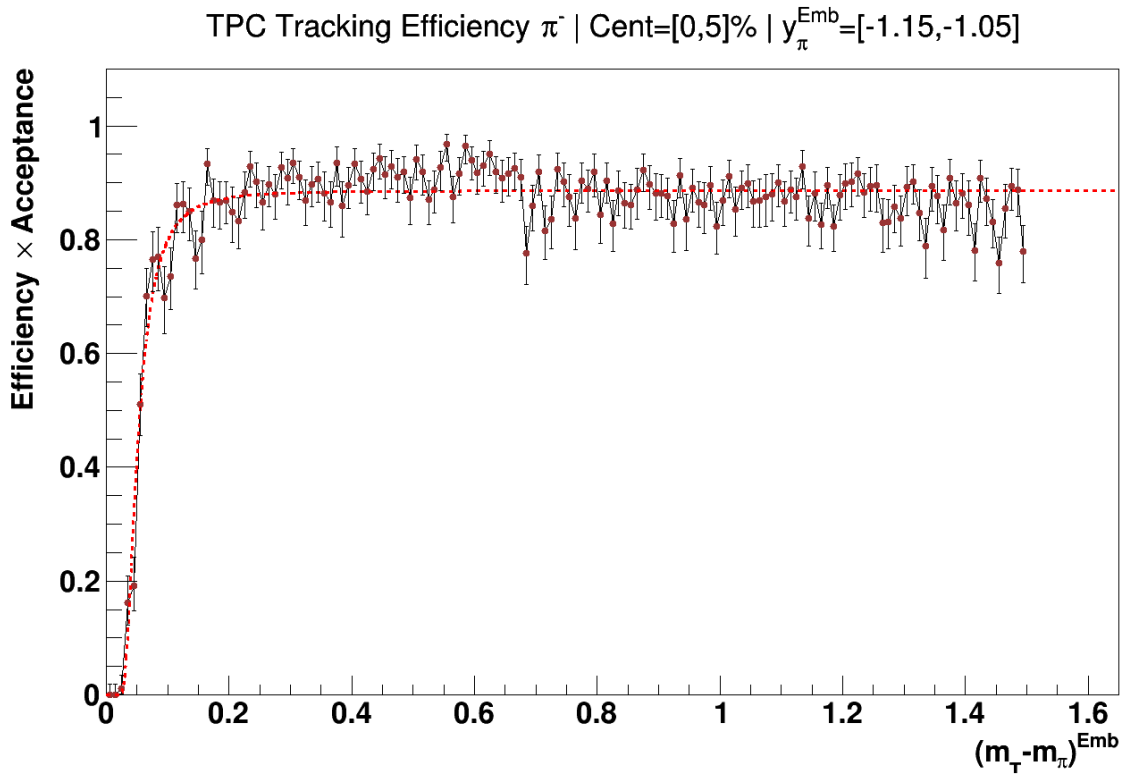


Figure 6.1: The efficiency fit to the ratio of matched tracks to embedded tracks for an example rapidity bin.

Chapter 7

Corrected Spectra

After applying the efficiency corrections, the corrected spectra for the π^- can now be plotted. This is done by taking the raw spectra and dividing each spectrum point by the the fitted efficiency value evaluated at the $m_T - m_{\pi^-}$ value corresponding to the bin center for each respective point.

7.1 Overall Systematic Errors for the Spectral Points

There are many sources of systematic errors in the yield extraction necessary for producing invariant mass spectra. The first source of systematic error comes from the track selection criteria. The number of hits and DCA requirements have been varied and this leads to a systematic error of 1%. The second source of systematic error comes from the choice of $n\sigma$ versus z_{TPC} . Both methodologies were used and it was found that the systematic differences in the obtained yield were 1.5%. The third source of systematic error comes from the estimation of the efficiency using embedded data. A systematic from the efficiency calculation was determined by taking the parameters of the function fit to the embedding data to their limits. This suggests a systematic error of about 3%. This methodology has been tested with data using the FastOffline data from the 3.0 GeV FXT run in 2018. FastOffline data is data that was taken during the run but has not yet gone through production.

This data driven methodology suggests the systematic error should be 5%, as shown in Figure 7.1. For the low $m_T - m_0$ region, the fit function fails. For some of these points, the

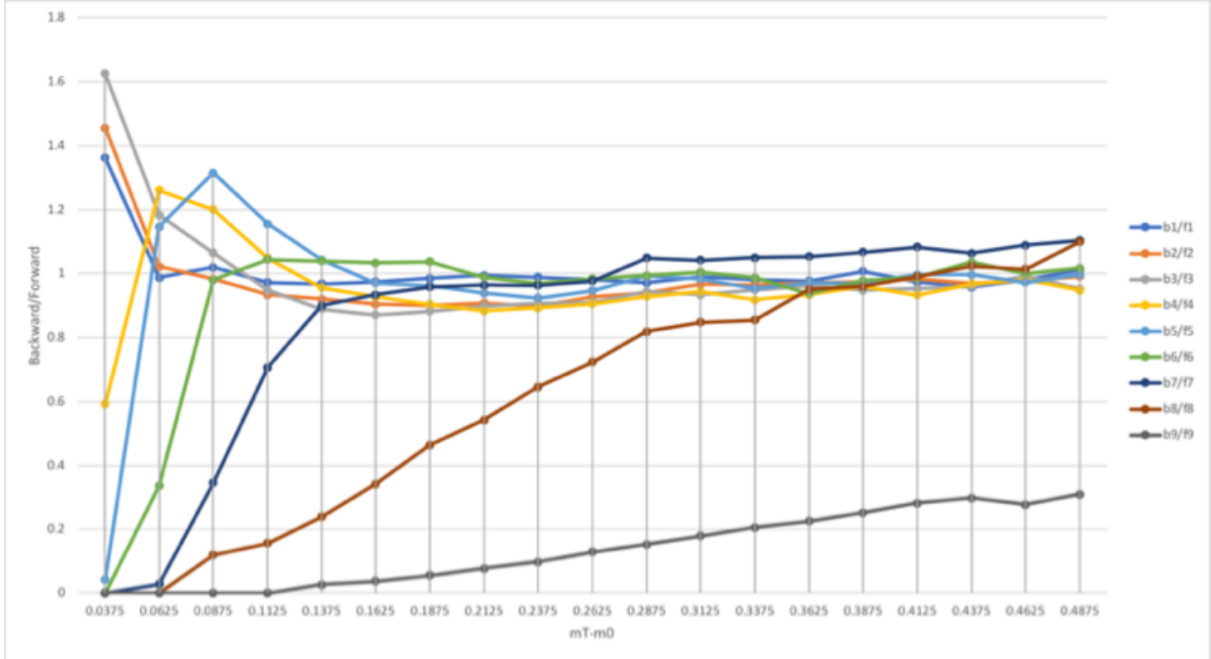


Figure 7.1: The yield ratio for pions rapidity slices equally spaced backward and forward of mid-rapidity for the 3.0 GeV Au+Au FXT system. These data are from the 2018 run. Physics requires the pion yields to be symmetric around mid-rapidity. Therefore the value of the backward/forward ratio is a measure of the systematic error in the efficiency correction. The systematic error in the efficiency correction is found to be 5% for higher $m_T - m_0$ bins.

systematic error is estimated from Figure 7.1, the data points are suppressed in the spectra where this estimated systematic error is greater than 50%. The fourth source of systematic error comes from the energy loss correction. This correction is not relevant for pions as the production software corrects all particles as if they were pions. For heavy particles, the energy loss correction is always less than 10%; the error in the correction is 0.5% of the yield. The fifth source of systematic error comes from the hadronic background correction. This background is the result of secondary interactions with the material between the target and the detector (mostly the beam pipe). This background correction is always less than 20%. The error in the background correction is 5%, resulting in a 1% systematic error in the yields. These error are tabulated in Table 7.1.

Table 7.1: Sources of systematic uncertainty

Source of error	maximum contribution (%)
Track Selection Cuts	1
$n\sigma$ vs. z_{TPC}	1.5
Efficiency	5
Energy Loss	0.5
Background	1
Total Error	5.43

Chapter 8

Rapidity Density Yields

8.1 Results

The raw yields are converted to an invariant yield by dividing by $1/(2\pi m_T)$ and the efficiency (ϵ), then normalized with respect to the transverse mass (dm_T) and rapidity (dy) bins and the number of events (N_{Event}). The pion spectra are fit with a double Bose-Einstein function,

$$f(m_T - m_0) = (dN/dy)_{\text{low}} A_{\text{low}} \frac{1}{(e^{m_T/T_{\text{low}}} - 1)} + (dN/dy)_{\text{high}} A_{\text{high}} \frac{1}{(e^{m_T/T_{\text{high}}} - 1)} \quad (8.1)$$

up to 1 GeV/c². This was used to separate the pions that were sourced from Delta resonances (low T) and ones thermally produced in the interaction zone (high T). This was done in a two round procedure - in the first round, a four parameter fit was applied to each rapidity slice for a given centrality. The low temperature parameter, T_{low} , from the double Bose-Einstein, was then fit to a constant over all rapidity for a given centrality. Likewise, the high temperature parameter, T_{high} from the double Bose-Einstein, was then fit using a Gaussian over all rapidity for a given centrality. The dN/dy_{low} parameter from the double Bose-Einstein was fit using a linear function over a narrower range of rapidity ($0.3 \lesssim y_{\text{lab}}/y_{\text{beam}} \lesssim 0.8$) for a given centrality. In the second round, the three previously mentioned parameters are then evaluated at each rapidity matching the respective rapidity slice and fixed. A final fit is then done with dN/dy_{high} as the only free parameter. The spectra points as a function of centrality is shown in Figure 8.1.

A somewhat similar procedure was done for the protons. The protons, after efficiency

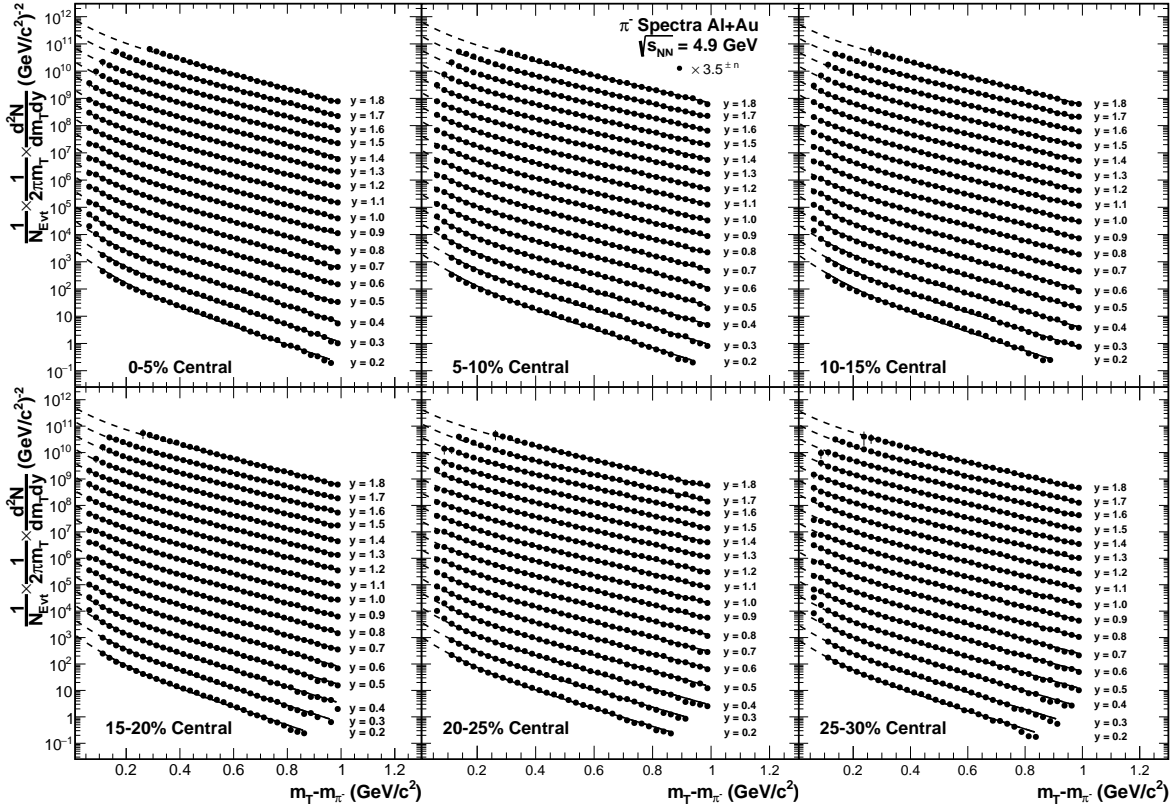


Figure 8.1: Invariant spectra of π^- for different rapidity and centrality classes from STAR FXT Al+Au collisions at $\sqrt{s_{NN}} = 4.9$ GeV. To make the plot more legible, the spectra are scaled by a factor of $3.5^{\pm n}$, where n is 0 for target-rapidity and increases by one for each successive rapidity slice (the rapidity are quoted in the laboratory frame). The data are fit with a double Bose-Einstein function. The fit function is displayed as a solid line where there are data and as a dashed line where extrapolated to low $m_T - m_0$.

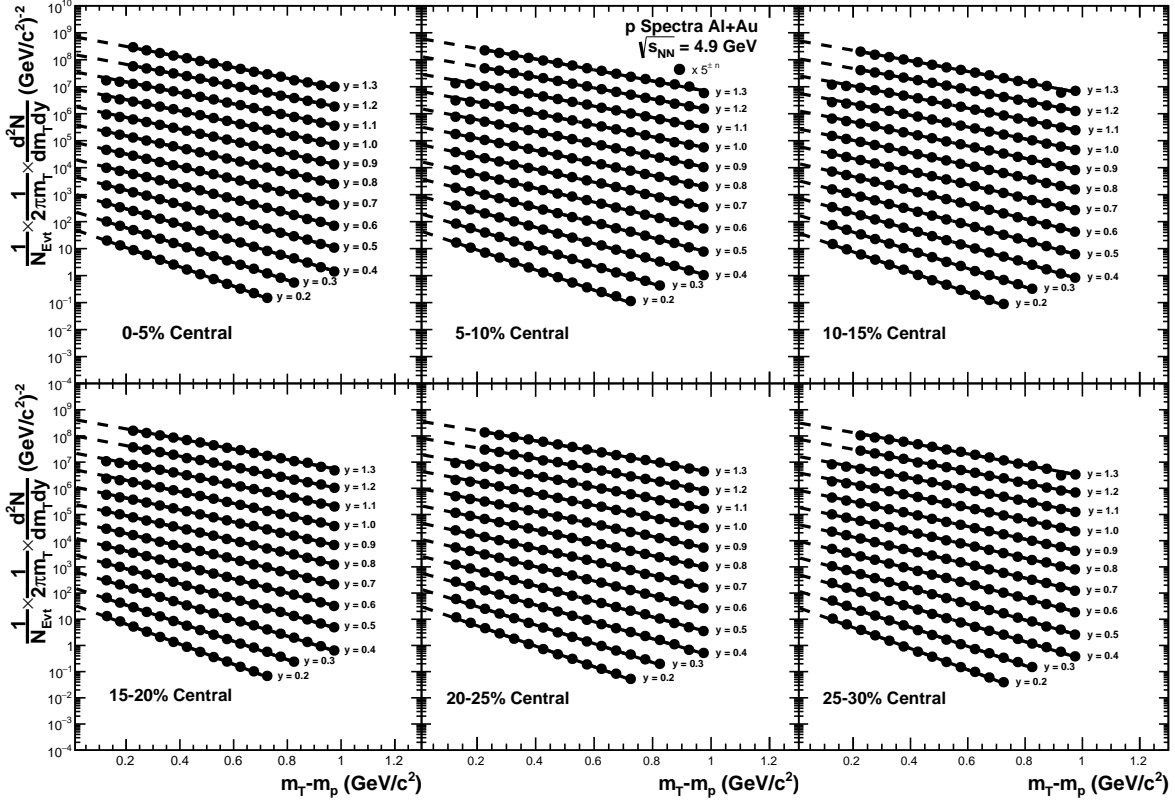


Figure 8.2: Invariant spectra of protons for different rapidity centrality classes from STAR FXT Al+Au collisions at $\sqrt{s_{NN}} = 4.9$ GeV. To make the plot more legible, the spectra are scaled by a factor of $5^{\pm n}$, where n is 0 for mid-rapidity. The data are extrapolated to low $m_T - m_0$ with a thermal fitting function.

corrections, were fit with a thermal fitting function, performed by Sam Heppelmann. This is shown in Figure 8.2.

8.2 Discussion of Systematic Uncertainties

The leading contribution of systematic uncertainty in the dN/dy for the π^- for each bin of rapidity is extrapolation of the yield to lower $m_T - m_0$. Furthermore, as the more forward rapidity bins do not reach as low in transverse mass, the systematic uncertainty is larger. Due to the geometry of the TPC, more forward tracks leave fewer hits in the TPC. In addition to thermal pions, many pions come from decays of Δ resonances around this energy of $\sqrt{s_{NN}} = 4.9$ GeV. At lower $m_T - m_0$, the dominant source of pions comes

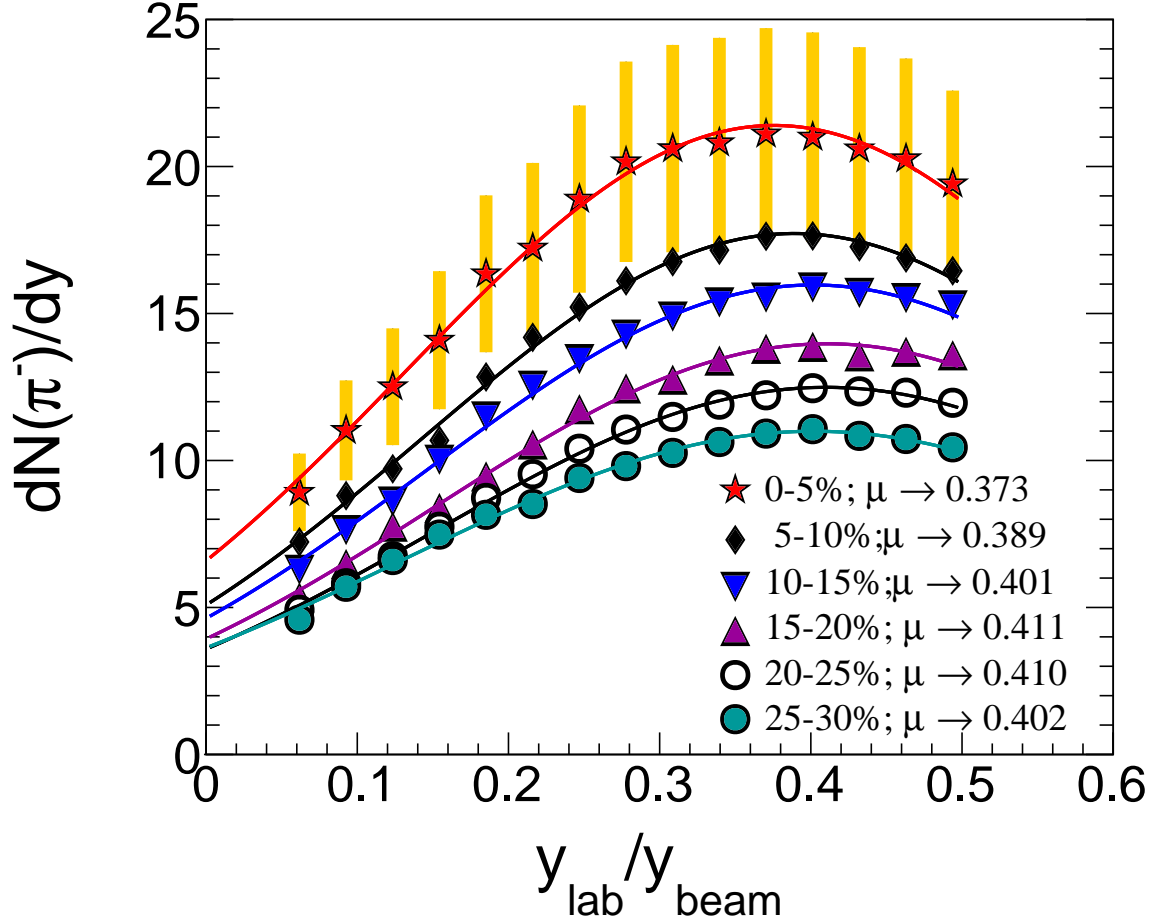


Figure 8.3: π^- rapidity density distributions for different centrality bins from Al+Au collisions at $\sqrt{s_{NN}} = 4.9$ GeV. The systematic error bars (yellow bars) are only shown for the 0-5% centrality bin; the relative errors for the other centralities are similar.

from Δ decays. At higher $m_T - m_0$, the dominant source of pions comes from thermal production. Due to this, a double Bose-Einstein, as mentioned in Equation 8.1, was used as the spectra fitting function, having both a low temperature and a high temperature component. The spectra were also fit with a double Maxwell-Boltzmann fit function and the resulting difference in dN/dy_{high} at each rapidity bin, for each centrality, was used as a systematic uncertainty.

Lastly, to obtain the systematic uncertainty in the mean $y_{\text{lab}}/y_{\text{beam}}$ of the π^- dN/dy_{high} , the rapidity distribution was first fit with a Gaussian and the amplitude and width parameters, initially free, became fixed after a two round process. In the first round, the

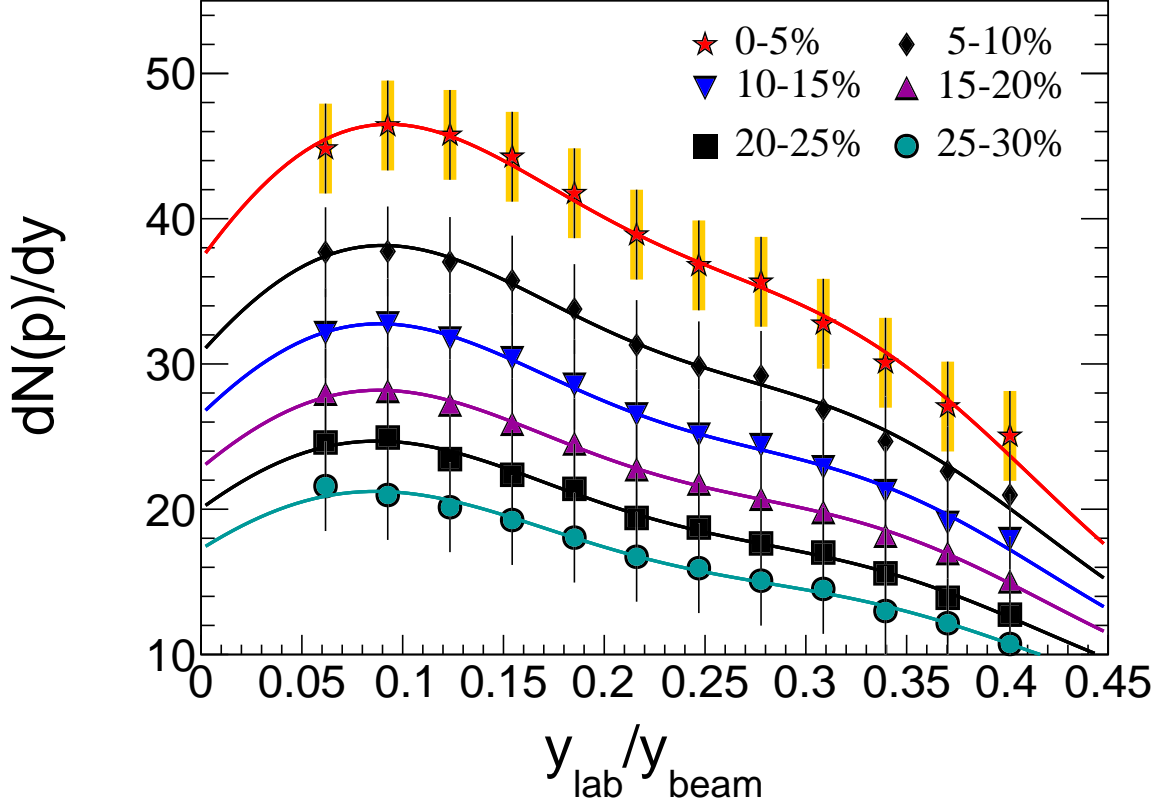


Figure 8.4: Proton rapidity density distributions for different centrality bins from Al+Au collisions at $\sqrt{s_{NN}} = 4.9$ GeV from STAR. Three Gaussians are used to fit the protons. One Gaussian describes the spectator protons from the Au target, another describes the participant protons from the Au target, and the last represents the participant protons from the Al projectile.

amplitude, mean, and width are free parameters. The width parameter is then plotted as a function of centrality and is fit with a constant to be used in the second round as a constant for all centralities. In the second round, the amplitude parameter is fixed using the respective amplitude parameter from the previous round (per centrality) and the width parameter is a fixed value for all centralities with only the mean as a free parameter. To find the uncertainty in the mean $y_{\text{lab}}/y_{\text{beam}}$ of the π^- dN/dy_{high} , the 0-5% centrality bin was used. The previously fixed amplitude was fixed to its previous value $\pm 5\%$ and, separately, the width parameter was fixed to its previous value $\pm 10\%$. The leading change in the mean $y_{\text{lab}}/y_{\text{beam}}$ suggested an uncertainty of ± 0.020 ($\sim 6\%$). This was then used as the systematic uncertainty for the mean $y_{\text{lab}}/y_{\text{beam}}$ of the π^- for all

centralities, as shown in Figure 8.3.

The process for the protons was similar. However, since the protons were fit with a triple Gaussian, there are more fixed parameters to vary. This is shown as a function of centrality in Figure 8.4. The 0-5% centrality bin was used and in using the same variations to the fixed parameters, the systematic uncertainty for the mean $y_{\text{lab}}/y_{\text{beam}}$ of the protons was found to be ± 0.010 ($\sim 3\%$). The Gaussians each represent a different contribution to the total dN/dy : one is from spectator protons from the gold target, another is participant protons from the gold target, and the third one is from participant protons from the aluminum projectile. Detail of the Gaussian fits for both the pions and the protons will be discussed in Chapter 9.

8.3 Comparison to Published Data

The results of the Al+Au $\sqrt{s_{NN}} = 4.9$ GeV can be compared to previous existing measurements of similar systems and energies. The (AGS) heavy ion program used $\sqrt{s_{NN}} = 5.4$ GeV silicon beams from 1992 to 1998. Results are available for π^- and protons from 0-7% centrality Si+Au collisions from the E802 experiment [6, 31, 32] and π^- and protons from the 0-9% centrality Si+Pb collisions from the E810 experiment [7, 8].

8.3.1 π^- Rapidity Density comparison

Focusing first on Figure 8.5, the STAR π^- rapidity density distributions from the 0-5% centrality bin are compared to the π^- rapidity distributions from the E802 and E810 experiments. There are some differences about the various sets of data that need to first be mentioned:

- Different $\sqrt{s_{NN}}$ - The silicon beam momentum used in AGS was a 14.7 AGeV, which corresponds to a $\sqrt{s_{NN}}$ of 5.4 GeV, a bit higher than the $\sqrt{s_{NN}} = 4.9$ GeV used for the current Al+Au results discussed in this work. This is relevant because the thermal pion yield typically scales linearly with $\log(\sqrt{s_{NN}})$ and therefore the expectation from this scaling is that the yield reported in this work should be 93% of that compared to the $\sqrt{s_{NN}} = 5.4$ GeV results.

- Centrality selection - The centrality used for the current results, 0-5%, are more

central than that of the previous results, 0-7% for E802, and 0-9% for E810. As the thermal pion production typically scales with the number of participating nucleons, $\langle N_{\text{part}} \rangle$, the centrality selection (and E810 used a Pb target) leads to the N_{part} being 3% lower for the AGS experiments. The $\langle N_{\text{part}} \rangle$ in Si+Au was 96.6 ± 4 . In Si+Pb, the $\langle N_{\text{part}} \rangle$ was 96.9 ± 4 .

- The difference in fits used to extract the respective pion yields - Both E802 and E810 used exponential fits to extract their respective pion yields. For the current analysis, a double Bose-Einstein function was used to fit the π^- spectra. Only the thermal part (high temperature component) of the pion spectra is used for this comparison. The use of a double Bose-Einstein versus that of an exponential fit function does change the integrated yield due to the low $m_T - m_0$ extrapolation. This low $m_T - m_0$ extrapolation makes up the leading contribution to the systematic errors estimated for the current data.

With these differences mentioned, the results from the Al + Au are observed to be consistent within uncertainties in both the amplitude and distribution shape with the previous E810 results. As for the comparison with E802, there is a discrepancy of one sigma, suggesting that the current analysis may have a centrality selection that is more central than 0-5%.

8.3.2 Proton Rapidity Density comparison

For the comparison of the protons, as shown in Figure 8.6, there are also differences in obtaining the yield. The discussion of yield scaling with $\log(\sqrt{s_{NN}})$ will not apply to the protons. This is because while the pions are primarily thermally created, most of the protons are not thermally created. The protons are created when the participant protons have stopped. There points that contribute to the differences in this comparison are:

- Centrality selection - The yield as a function of N_{part} does contribute for the protons.
- The difference in fits used to extract the pion yields - The AGS results for the protons, like the π^- , also used an exponential fit for the yield. The current results use a thermal fit and the systematic error from the low $m_T - m_0$ extrapolation is due to the small amount of radial flow.
- The $y_{\text{lab}}/y_{\text{beam}}$ normalization - The integrated 4π yield should be comparable to the

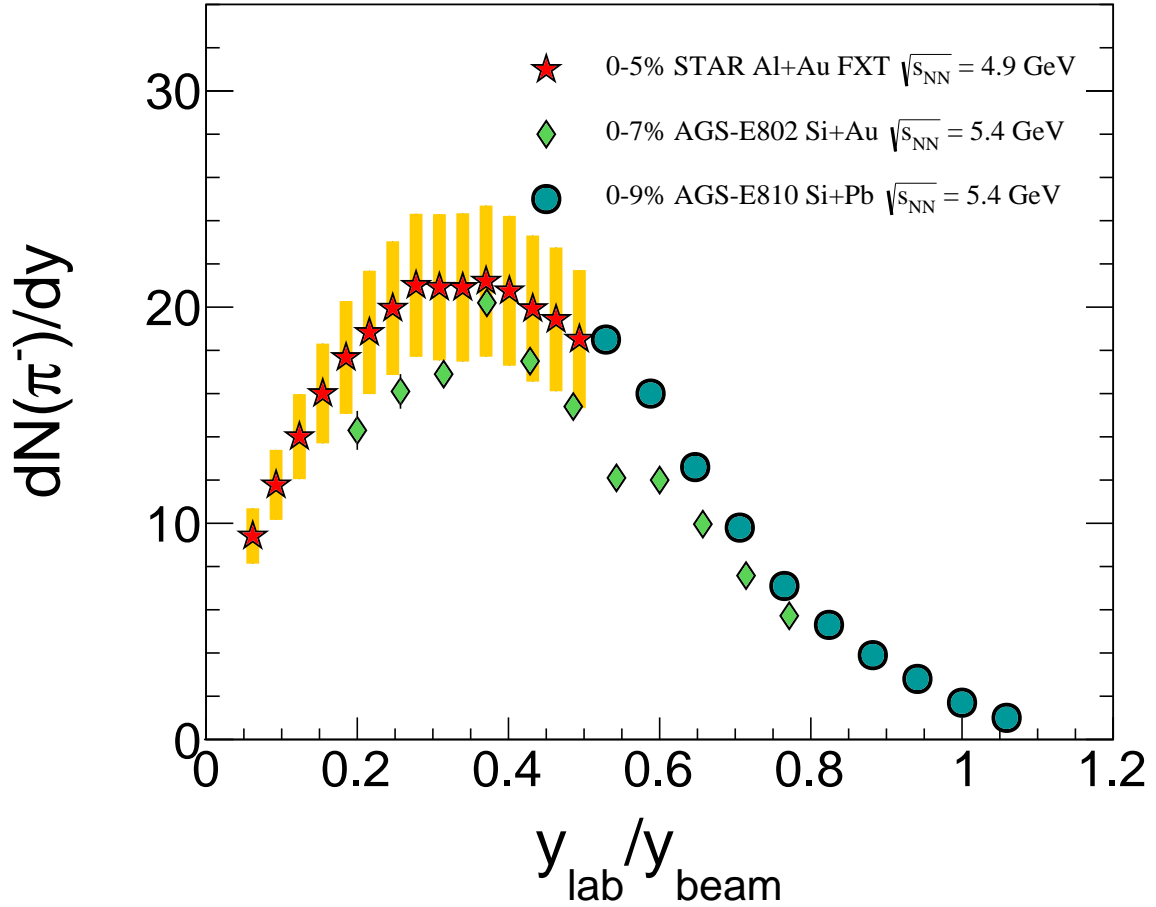


Figure 8.5: A comparison of the π^- rapidity density distribution (0-5%) with collisions at $\sqrt{s_{NN}} = 5.4$ GeV from the E802 (Si+Au, 0-7%) [6] and E810 (Si+Pb, 0-9%) [7, 8] experiments at the AGS. Systematic errors are shown as yellow bars.

number of participating protons. Because the observed yield of anti-protons is negligible, this indicates that the contribution of produced protons should also be negligible compared to participating protons. The rapidity of the silicon beam was 7% larger and this means that the normalization will suppress the previous AGS results by 7% in this comparison to current results.

Similar to that of the comparison between the π^- from the current results and E802, there is also a one sigma increase in the dN/dy of the protons from the Al + Au compared to that of E802.

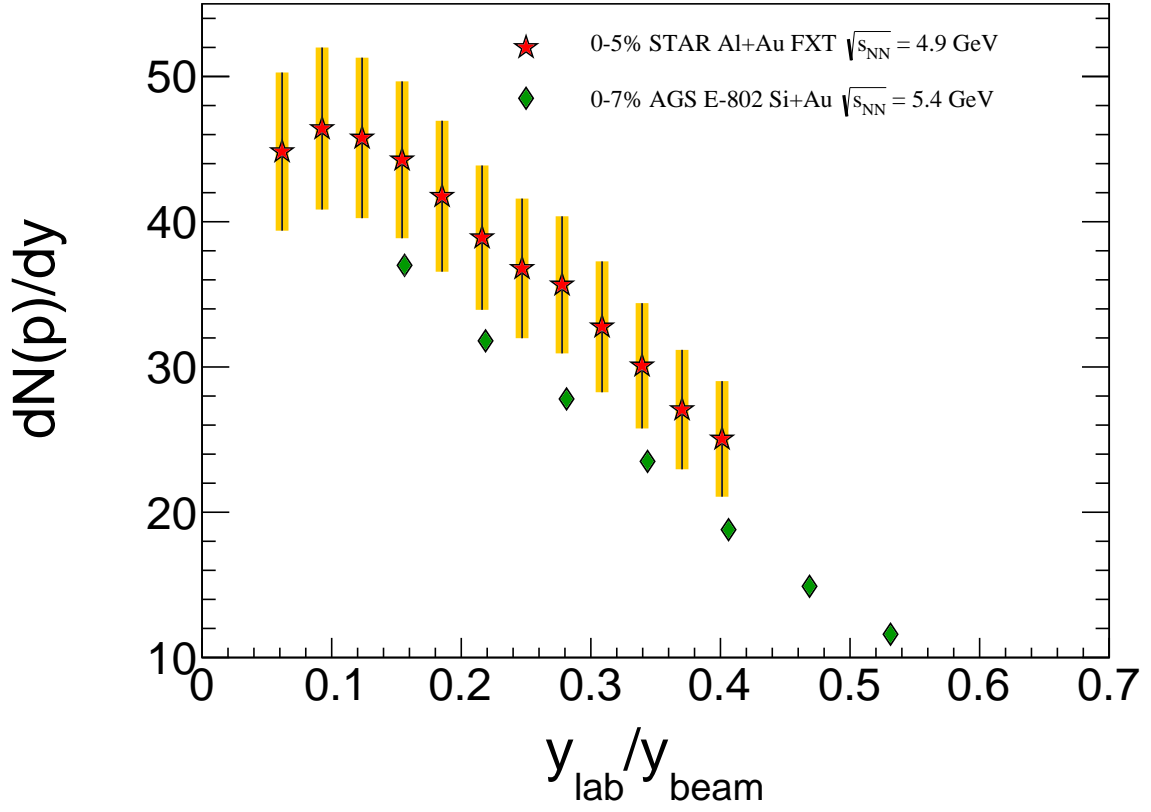


Figure 8.6: Comparison of the proton rapidity density distributions with (0-7%) Si+Au collisions at $\sqrt{s_{NN}} = 5.4$ GeV from E802 [6]. Systematic errors are shown as yellow bars.

Chapter 9

Discussion of Baryon Stopping

Baryon stopping is defined as either the rapidity loss of projectile baryons or the rapidity gain of target baryons. If the momentum of an incoming baryon only has transverse momentum in the final state of the baryon, it is completely stopped. Focusing on the peaks of the rapidity density distributions will allow for a way to measure the amount of baryon stopping. The rapidity of the thermal reference frame, or the interaction zone (IZ), is the region over which the Al and Au interact. It is able to be calculated by $y_{IZ} = \frac{1}{2} \ln \left(\frac{E+p_z}{E-p_z} \right)$ where E and p_z are respectively the energy and longitudinal momentum of the interaction zone. The values can be calculated from

$$E = \langle N_{\text{part}}^{\text{Al}} \rangle E^{\text{beam}} + \langle N_{\text{part}}^{\text{Au}} \rangle m_{\text{nucleon}} \quad (9.1)$$

$$p_z = \langle N_{\text{part}}^{\text{Al}} \rangle p_z^{\text{beam}} \quad (9.2)$$

where $E^{\text{beam}} = 11.73 \text{ GeV}$, $p_z^{\text{beam}} = 11.69 \text{ GeV}/c$, $m_{\text{nucleon}} = 0.9315 \text{ GeV}/c^2$ and the $\langle N_{\text{part}}^{\text{Al}} \rangle$ and $\langle N_{\text{part}}^{\text{Au}} \rangle$ values can be found in Table 4.1. Though the values of $\langle N_{\text{part}}^{\text{Al}} \rangle$ do not vary too much, the $\langle N_{\text{part}}^{\text{Au}} \rangle$ values do due to the aluminum nucleus essentially always being engulfed at these centralities (and therefore participating) and the larger gold nucleus having less participating nucleons as the centrality becomes more peripheral. This will mean that the interaction zone energy and momentum are centrality dependent. The changing values of the participating nucleons across the different centralities leads to the rapidity of the interaction zone varying across centrality as well. For this body of work,

the protons act as a proxy for baryons in the context of baryon stopping.

However, before discussing the protons, consider the pions. The reason for considering the pions, which are mesons, is that the peaks of these centrality bin distributions, shown in Figure 8.3, bins are always below 0.5 in units of y_{lab}/y_{beam} . The pions are peaked below 0.5 units of rapidity and the pions follow that of interaction zone rapidity.

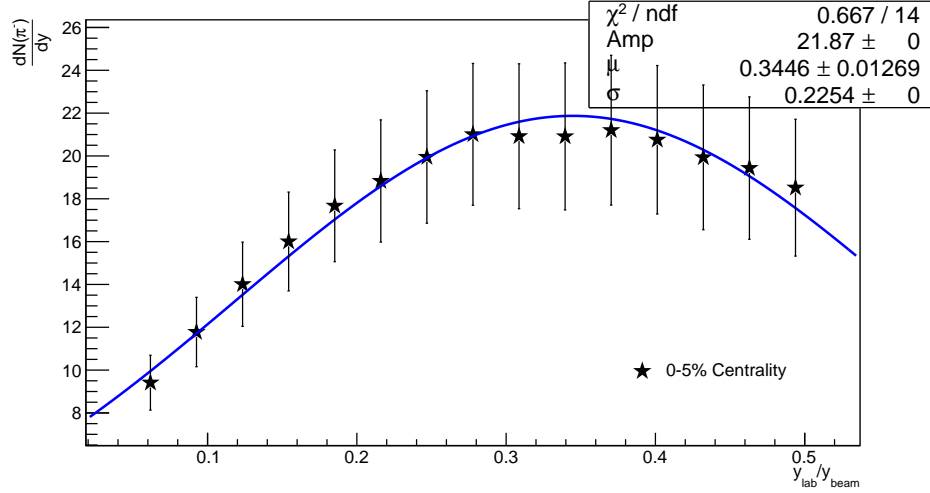


Figure 9.1: π^- rapidity density distributions for 0-5% centrality from Al+Au collisions at $\sqrt{s_{NN}} = 4.9$ GeV.

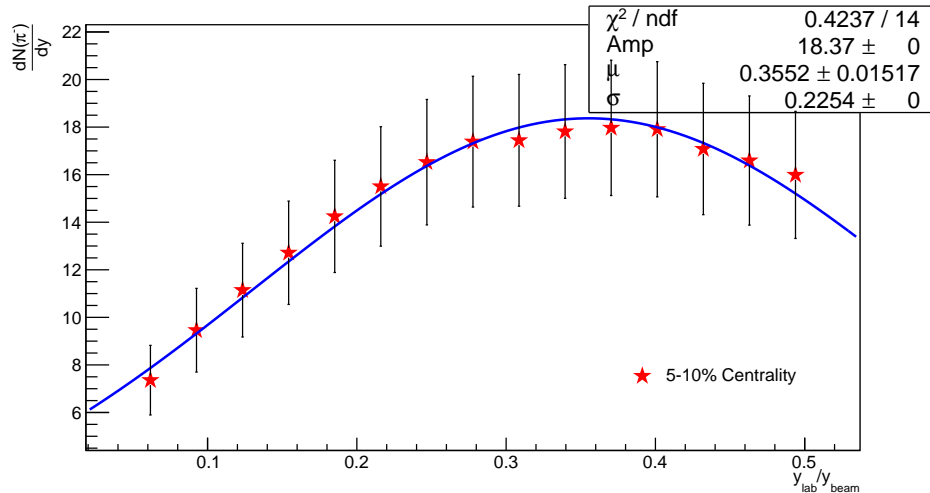


Figure 9.2: π^- rapidity density distributions for 5-10% centrality from Al+Au collisions at $\sqrt{s_{NN}} = 4.9$ GeV.

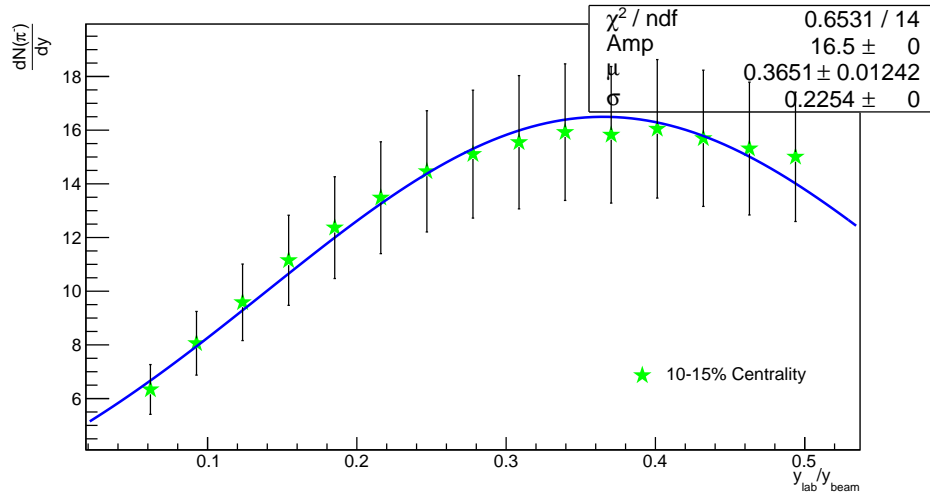


Figure 9.3: π^- rapidity density distributions for 10-15% centrality from Al+Au collisions at $\sqrt{s_{NN}} = 4.9$ GeV.

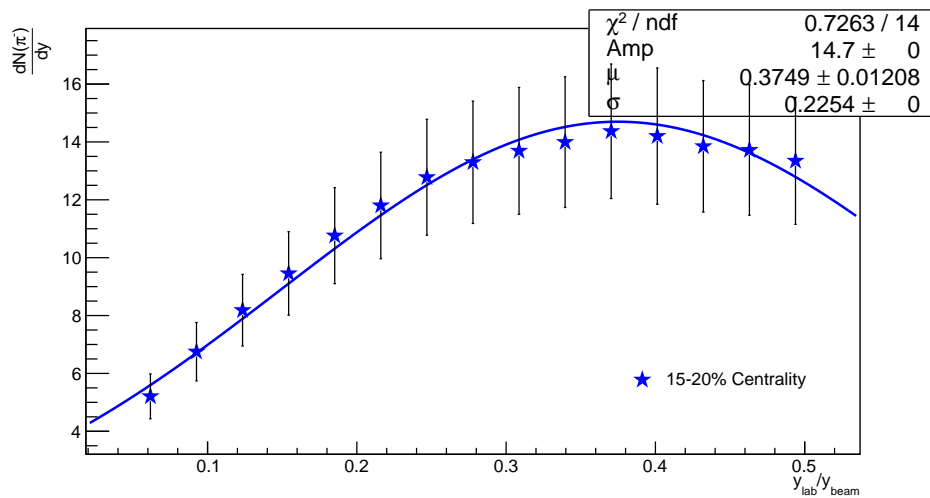


Figure 9.4: π^- rapidity density distributions for 15-20% centrality from Al+Au collisions at $\sqrt{s_{NN}} = 4.9$ GeV.

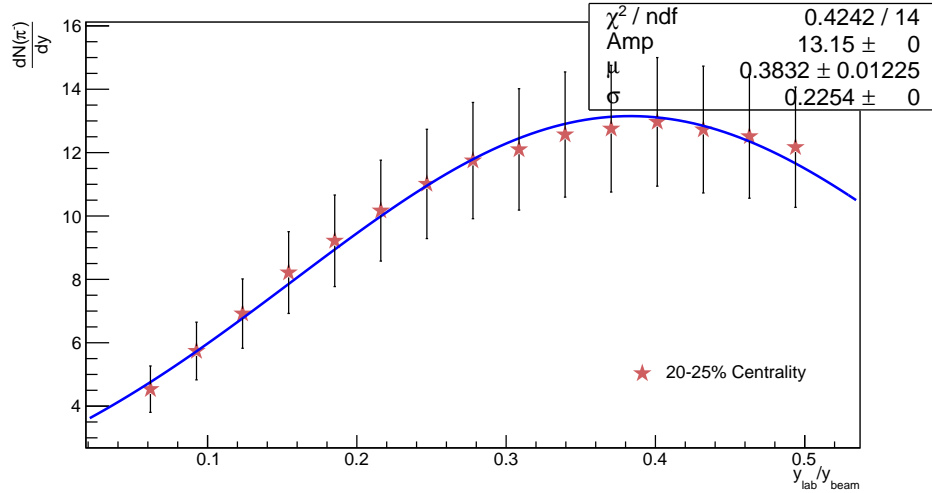


Figure 9.5: π^- rapidity density distributions for 20-25% centrality from Al+Au collisions at $\sqrt{s_{NN}} = 4.9$ GeV.

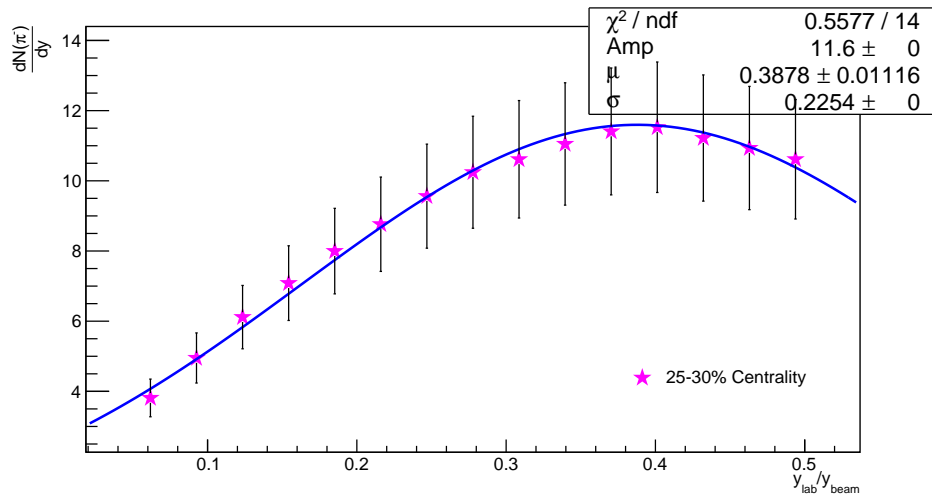


Figure 9.6: π^- rapidity density distributions for 25-30% centrality from Al+Au collisions at $\sqrt{s_{NN}} = 4.9$ GeV.

This is because the gold target contributes more nucleons than the aluminum beam. The fits to the pion rapidity distributions for each centrality are shown in Figures 9.1, 9.2, 9.3, 9.4, 9.5, and 9.6, respectively, for centralities 0-5%, 5-10%, 10-15%, 15-20%, 20-25%, and 25-30%.

To describe the protons, note that there is a multi-peak structure in the rapidity density distribution (unlike the single peaked pions). The peaks of this structure for any of the previously mentioned centralities correspond to the spectator protons from the gold target, the participating protons from the gold target, and the participating protons from the aluminum beam. The spectator protons, which are protons that are not part of the interaction, are much closer to that of the rapidity of the gold target. Then there are the participant protons, those which are the protons that were involved in an interaction.

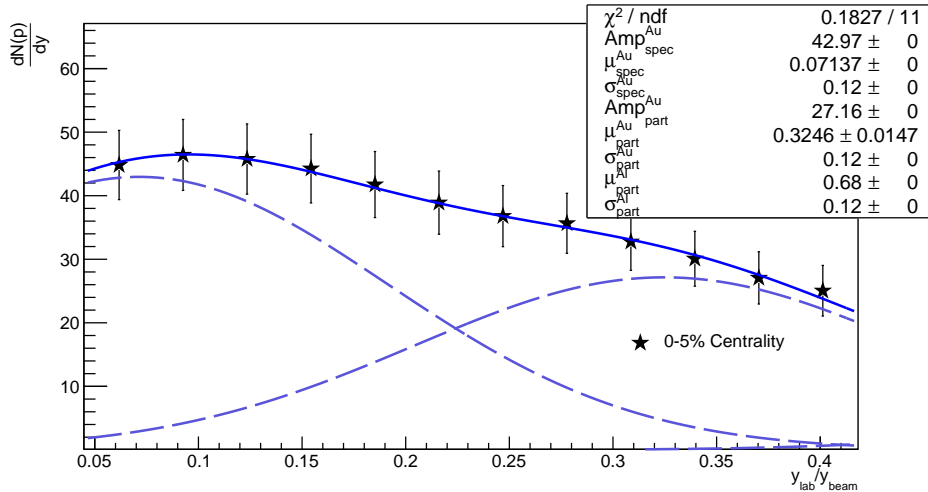


Figure 9.7: Proton rapidity density distributions for 0-5% centrality from Al+Au collisions at $\sqrt{s_{NN}} = 4.9$ GeV. The solid line represents the triple Gaussian fit. The dashed lines represent the individual Gaussian fits that correspond to the Au target spectator protons, Au target participant protons, and Al beam participant protons.

Each of the distributions across each centrality was fit with a triple Gaussian. The first Gaussian, peaked around $y_{\text{lab}}/y_{\text{beam}} = 0.07$, represents the spectator protons from the gold target. The second Gaussian, peaked at around $y_{\text{lab}}/y_{\text{beam}} = 0.33$, represents the participating protons from the gold target. And the third Gaussian, peaked at $y_{\text{lab}}/y_{\text{beam}} = 0.68$, represents the participating protons from the aluminum beam. The sum of the three

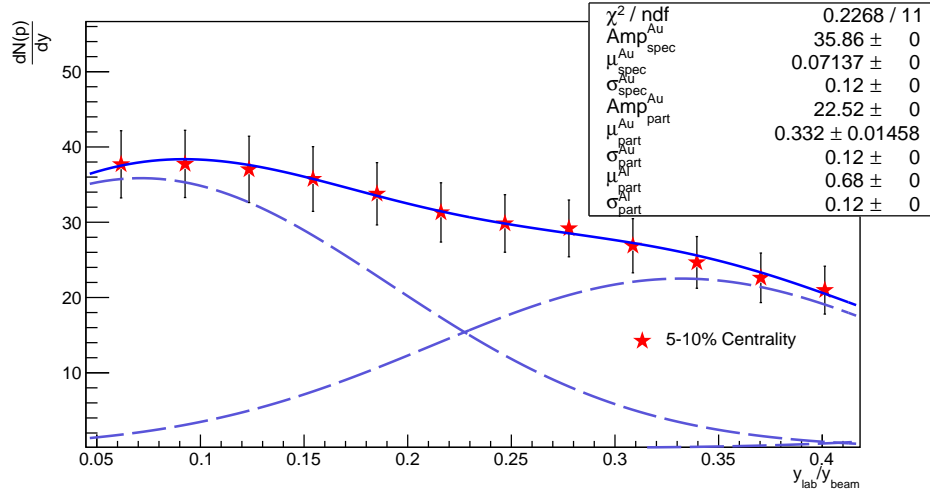


Figure 9.8: Proton rapidity density distributions for 5-10% centrality from Al+Au collisions at $\sqrt{s_{NN}} = 4.9$ GeV. The solid line represents the triple Gaussian fit. The dashed lines represent the individual Gaussian fits that correspond to the Au target spectator protons, Au target participant protons, and Al beam participant protons.

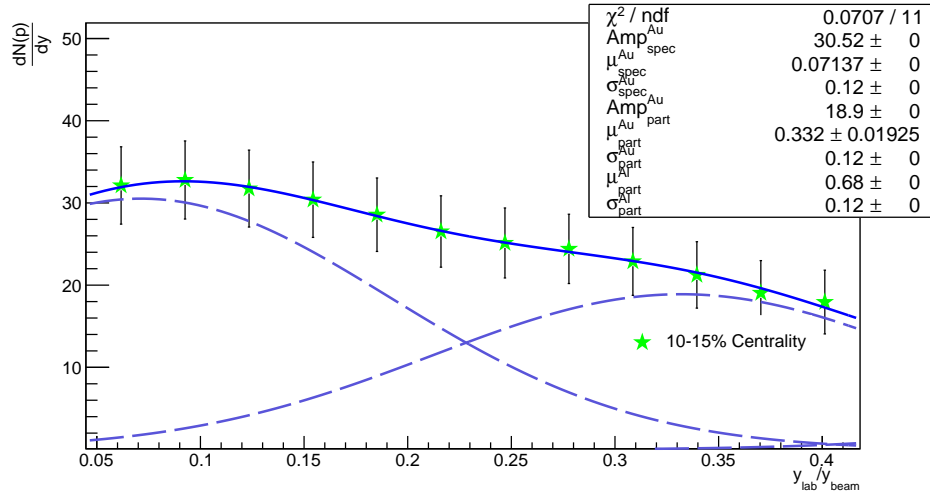


Figure 9.9: Proton rapidity density distributions for 10-15% centrality from Al+Au collisions at $\sqrt{s_{NN}} = 4.9$ GeV. The solid line represents the triple Gaussian fit. The dashed lines represent the individual Gaussian fits that correspond to the Au target spectator protons, Au target participant protons, and Al beam participant protons.

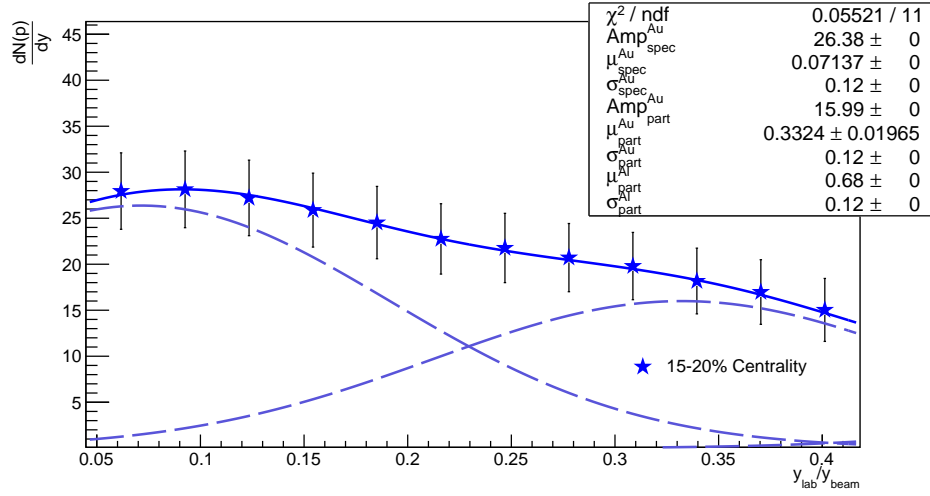


Figure 9.10: Proton rapidity density distributions for 15-20% centrality from Al+Au collisions at $\sqrt{s_{NN}} = 4.9$ GeV. The solid line represents the triple Gaussian fit. The dashed lines represent the individual Gaussian fits that correspond to the Au target spectator protons, Au target participant protons, and Al beam participant protons.

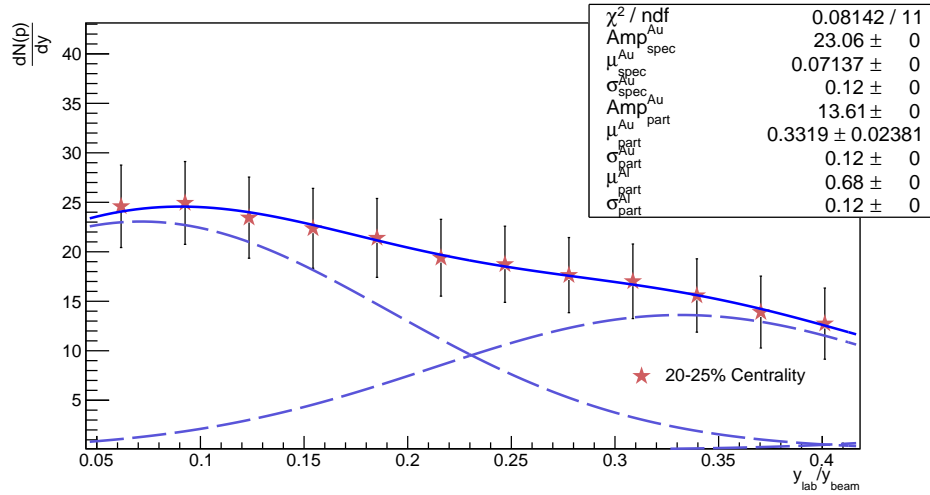


Figure 9.11: Proton rapidity density distributions for 20-25% centrality from Al+Au collisions at $\sqrt{s_{NN}} = 4.9$ GeV. The solid line represents the triple Gaussian fit. The dashed lines represent the individual Gaussian fits that correspond to the Au target spectator protons, Au target participant protons, and Al beam participant protons.

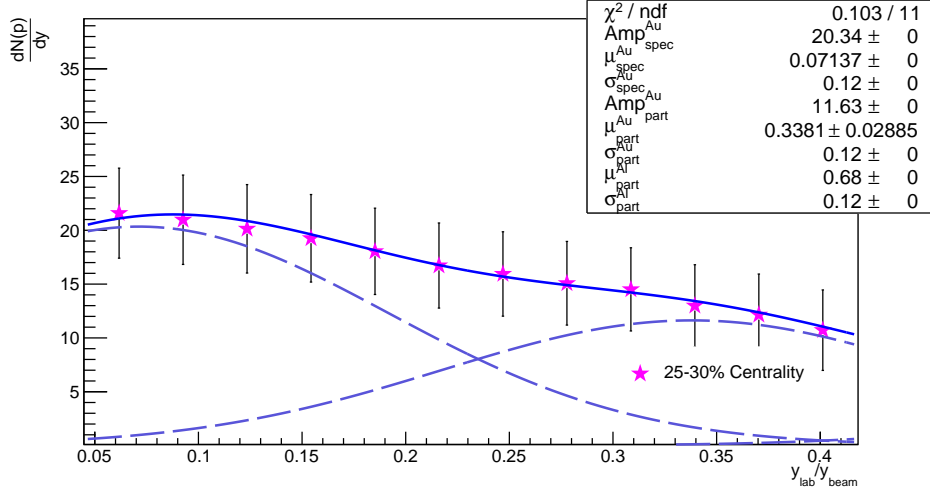


Figure 9.12: Proton rapidity density distributions for 25-30% centrality from Al+Au collisions at $\sqrt{s_{NN}} = 4.9$ GeV. The solid line represents the triple Gaussian fit. The dashed lines represent the individual Gaussian fits that correspond to the Au target spectator protons, Au target participant protons, and Al beam participant protons.

Gaussians may be written as

$$\begin{aligned}
 f(x) = & [p_0] \exp\left(-\frac{1}{2} \left(\frac{x - [p_1]}{[p_2]}\right)^2\right) + [p_3] \exp\left(-\frac{1}{2} \left(\frac{x - [p_4]}{[p_5]}\right)^2\right) \\
 & + [p_3] \frac{\langle N_{part}^{Au} \rangle}{\langle N_{part}^{Al} \rangle} \exp\left(-\frac{1}{2} \left(\frac{x - [p_6]}{[p_7]}\right)^2\right)
 \end{aligned} \tag{9.3}$$

where $x \equiv y_{lab}/y_{beam}$, $[p_0]$ is the gold spectator amplitude, $[p_1]$ is the mean y_{lab}/y_{beam} of the gold spectator protons, $[p_2]$ is the gold spectator width, $[p_3]$ is the gold participant amplitude, $[p_4]$ is the mean y_{lab}/y_{beam} of the gold participant protons, $[p_5]$ is the gold participant width, $[p_6]$ is the mean y_{lab}/y_{beam} of the aluminum participant protons, and $[p_7]$ is the aluminum participant width. The ratio of the aluminum participant amplitude and gold participant amplitude is fixed to that of the ratio of participating nucleons (where this ratio varies across centrality). These fits to the proton rapidity density distributions are shown in Figures 9.7, 9.8, 9.9, 9.10, 9.11, and 9.12, respectively, for centralities 0-5%, 5-10%, 10-15%, 15-20%, 20-25%, and 25-30%. The solid line on each of these figures represents the overall fit, as mentioned in Equation 9.3. The dashed lines represent the individual Gaussian fits. The peak of the dashed lines correspond to the locations of the mean from the triple Gaussian fit to the spectator protons from the gold target and the

participant protons from the gold target. The peak of the dashed line corresponding to the participant protons from the aluminum beam is not shown, as it is off the axis and the data does not extend to those values of $y_{\text{lab}}/y_{\text{beam}}$. Table 9.1 summarizes the centrality dependence of the interaction zone rapidity, the mean fit to the pion rapidity distributions (μ_{π^-}), and the mean fit to the proton rapidity distributions (μ_p). The interaction zone rapidity, $y_{IZ} = \frac{1}{2} \ln \left(\frac{E+p_z}{E-p_z} \right)$, is calculated from Equations 9.1 and 9.2.

Table 9.1: Mean $y_{\text{lab}}/y_{\text{beam}}$ of the Gaussian fit to the dN/dy distributions for pions (μ_{π^-}) and protons (μ_p) for different centralities. The y_{IZ}/y_{beam} represents the fraction of the interaction zone rapidity to the beam rapidity.

Centrality (%)	y_{IZ}/y_{beam}	μ_{π^-}	μ_p
0 - 5	0.354	$0.345 \pm 0.013 \pm 0.020$	$0.325 \pm 0.015 \pm 0.010$
5 - 10	0.371	$0.355 \pm 0.015 \pm 0.020$	$0.332 \pm 0.015 \pm 0.010$
10 - 15	0.389	$0.365 \pm 0.012 \pm 0.020$	$0.332 \pm 0.019 \pm 0.010$
15 - 20	0.400	$0.375 \pm 0.012 \pm 0.020$	$0.332 \pm 0.020 \pm 0.010$
20 - 25	0.412	$0.383 \pm 0.012 \pm 0.020$	$0.332 \pm 0.024 \pm 0.010$
25 - 30	0.422	$0.388 \pm 0.011 \pm 0.020$	$0.338 \pm 0.029 \pm 0.010$

Figure 9.13 shows the mean $y_{\text{lab}}/y_{\text{beam}}$ as a function of centrality for the π^- and the protons. The values in this figure are given in Table 9.1. The π^- mean $y_{\text{lab}}/y_{\text{beam}}$ tend to larger values for more peripheral events and this is consistent with the trend of the interaction zone rapidity. This suggests that the pions are thermally produced in the equilibrated interaction zone. As a reminder, the dN/dy values of the high temperature component of the π^- and not the low $m_T - m_0$ component that comes from the decays of Δ resonances. From Table 9.1, the average mean for the protons across centrality is $\langle \mu_p \rangle = 0.332 \pm 0.007 \pm 0.010$ in units of $y_{\text{lab}}/y_{\text{beam}}$. Converting this to lab rapidity by multiplying by $y_{\text{beam}} = 3.225$ gives the stopping for the participating gold nucleons to be $\delta y = 1.071 \pm 0.023 \pm 0.032$ units. The effective nuclear thickness of the projectile as perceived by the target nucleons does not significantly change with centrality; therefore, it is not unexpected that the stopping of the Au nucleons is independent of centrality. The δy values observed in this work for the participating nucleons are consistent with the

value found for the silicon projectile nucleons in Si+Al collisions at the same energy [42].

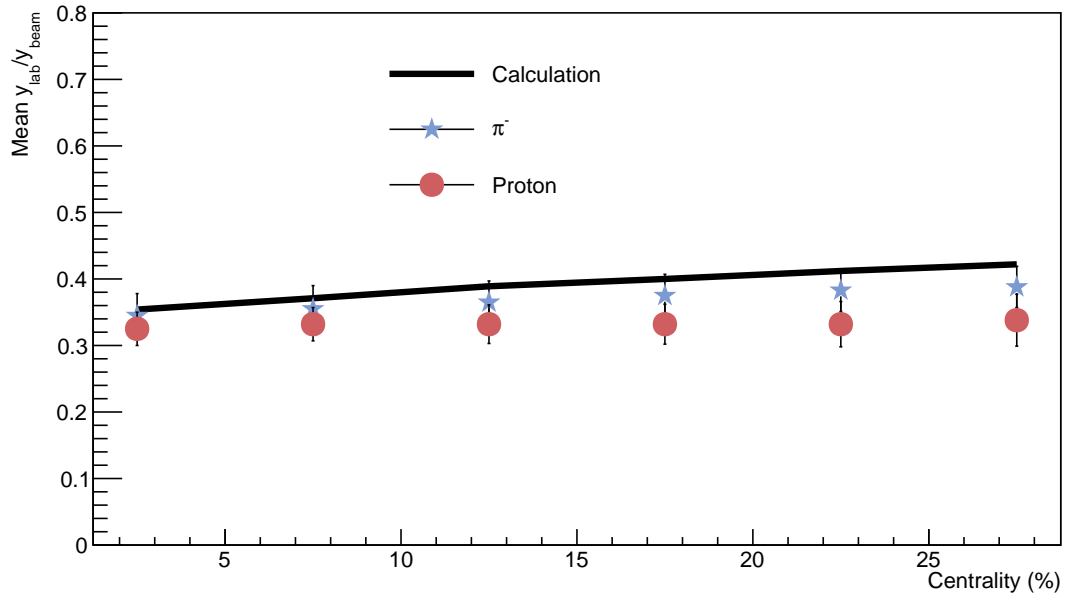


Figure 9.13: Mean π^- and proton $y_{\text{lab}}/y_{\text{beam}}$ as a function of centrality. The black line is the calculation of the mean interaction zone rapidity, $y_{\text{IZ}}/y_{\text{beam}}$, as a function of centrality from Table 9.1.

Chapter 10

Conclusion

This dissertation covers the analysis and results from π^- and proton spectra and rapidity densities from Al + Au fixed-target collisions at $\sqrt{s_{NN}} = 4.9$ GeV from the STAR experiment in 2015. Comparing to previously published data, there is consistency between the π^- and proton yields measured by E802 and E810 at AGS and the current data (with acknowledgement of a one sigma increase in the current data compared to that of E802). As seen in Figure 9.13, the mean y_{lab}/y_{beam} of the high temperature component of the π^- , as a function of centrality, are consistent with the interaction zone rapidity suggesting that the pions are thermally produced in an equilibrated interaction zone. The proton rapidity distributions include the contributions from the target spectator, target participant, and projectile participant components. The target participant is used to estimate the baryon stopping, δy , of the gold nucleons. This is calculated to be $\delta y = 1.071 \pm 0.023 \pm 0.032$ units. This means that at these energies, we are in a more baryon-rich regime (higher μ_B values) than at higher energies (lower μ_B values).

These results mentioned in this dissertation are just part of a major collaborative effort that has successfully found results consistent with the AGS experiments. In addition to the Au + Au fixed-target collisions at $\sqrt{s_{NN}} = 4.5$ GeV test run, this analysis has demonstrated that a fixed-target program in a collider is feasible and has played a role in making the FXT program part of BES-II. Since the data involved in this dissertation has been taken, many more runs have been collected, with energies as low as $\sqrt{s_{NN}} = 3.0$ GeV and as high as $\sqrt{s_{NN}} = 7.7$ GeV. The author of this work is appreciative of

having the opportunity to have had a role in development of the STAR FXT program by working on this second set of data taken during the pilot run.

REFERENCES

- [1] R. Snellings. Elliptic flow: a brief review. *New Journal of Physics*, 13:055008, 2011. doi: 10.1088/1367-2630/13/5/055008. URL <https://iopscience.iop.org/article/10.1088/1367-2630/13/5/055008/pdf>.
- [2] M. Gyulassy and L. McLerran. New Forms of QCD Matter Discovered at RHIC. *Nucl. Phys. A*, 750:30-63, 2005. doi: 10.1016/j.nuclphysa.2004.10.034. URL <https://arxiv.org/pdf/nucl-th/0405013.pdf>.
- [3] M. Anderson *et al.* The STAR time projection chamber: A Unique tool for studying high multiplicity events at RHIC. *Nucl. Instrum. Meth.*, A499:659–678, 2003. doi: 10.1016/S0168-9002(02)01964-2.
- [4] P. Fachini *et al.* Proposal for a Large Area Time of Flight System for STAR. *STAR Note*, SN0621:56, 2004. URL <https://drupal.star.bnl.gov/STAR/files/tof-5-24-2004.pdf>.
- [5] F. Geurts *et al.* Performance of the Prototype MRPC detector for STAR. *Nuclear Instruments and Methods in Physics Research Section A*, 533:56, 2004. doi: 10.1016/j.nima.2004.07.001. URL <https://drupal.star.bnl.gov/STAR/files/tof-5-24-2004.pdf>.
- [6] T. Abbott *et al.* Charged hadron distributions in central and peripheral Si + A collisions at 14.6-AGeV/c. *Phys. Rev.*, C50:1024–1047, 1994. doi: 10.1103/PhysRevC.50.1024.
- [7] S. E. Eiseman *et al.* Rapidity distributions and nuclear transparency in heavy ion collisions. *Phys. Lett.*, B292:10–12, 1992. doi: 10.1016/0370-2693(92)90600-9.
- [8] E. Efstathiadis and R. Longacre. Charged Particle Production from E810, 1995.
- [9] D. J. Gross and F. Wilczek. Ultraviolet Behavior of Non-Abelian Gauge Theories. *Phys. Rev. Letters*, 30:1343, 1973. URL <https://journals.aps.org/prl/pdf/10.1103/PhysRevLett.30.1343>.

- [10] H. D. Politzer. Reliable Perturbative Results for Strong Interactions? *Phys. Rev. Letters*, 30:1346, 1973. URL <https://journals.aps.org/prl/pdf/10.1103/PhysRevLett.30.1346>.
- [11] D. J. Gross and F. Wilczek. Asymptotically free gauge theories. I. *Phys. Rev. D*, 8:3633, 1973. URL <https://journals.aps.org/prd/pdf/10.1103/PhysRevD.8.3633>.
- [12] H. D. Politzer. Asymptotic Freedom: An Approach to Strong Interactions. *Phys. Rep*, 14:129, 1974. URL http://puhep1.princeton.edu/~kirkmcd/examples/EP/politzer_pr_14_129_74.pdf.
- [13] CERNpress. TNew state of matter created at CERN, 2000. URL <https://home.cern/news/press-release/cern/new-state-matter-created-cern>.
- [14] PHOBOS Collaboration, STAR Collaboration, PHOENIX Collaboration, BRAHMS Collaboration. Hunting the Quark Gluon Plasma: Results from the first 3 years at RHIC. *Brookhaven National Laboratory Formal Report*, Apr 2005. URL <https://www.bnl.gov/isd/documents/29263.pdf>.
- [15] P. Steinberg. First results from the LHC heavy ion program. *New Journal of Physics*, 14:035006, Mar 2012. doi: 10.1088/1367-2630/14/3/035006. URL <https://iopscience.iop.org/article/10.1088/1367-2630/14/3/035006/pdf>.
- [16] P. Kolb and U. Heinz. Hydrodynamic description of ultrarelativistic heavy-ion collisions. pages 634–714, 2005. URL <https://arxiv.org/pdf/nucl-th/0305084.pdf>.
- [17] Y. Aoki *et al.* The order of the quantum chromodynamics transition predicted by the standard model of particle physics. *Nature*, 443:675-678, 2006. doi: 10.1038/nature05120. URL <https://arxiv.org/pdf/hep-lat/0611014.pdf>.
- [18] Bhattacharya *et al.* (HotQCD Collaboration). The QCD phase transition with physical-mass, chiral quarks. *Phys. Rev. Letters*, 113:082001, 2014. doi: 10.1103/PhysRevLett.113.082001. URL <https://arxiv.org/pdf/1402.5175.pdf>.

- [19] D. H. Rischke. The Quark-Gluon Plasma in Equilibrium. *Prog. Part. Nucl. Phys.*, 52:197-296, 2004. doi: 10.1016/j.ppnp.2003.09.002. URL <https://arxiv.org/pdf/nucl-th/0305030.pdf>.
- [20] M. A. Stephanov. QCD phase diagram and the critical point. *Int. J. Mod. Phys. A*, 20:43874392, 2005. doi: 10.1142/S0217751X05027965. URL <https://arxiv.org/pdf/hep-ph/0402115.pdf>.
- [21] K. Fukushima and C. Sasak. The phase diagram of nuclear and quark matter at high baryon density. *Prog. Part. Nucl. Phys.*, 72:99154, 2013. doi: 10.1016/j.ppnp.2013.05.003. URL <https://arxiv.org/pdf/1301.6377.pdf>.
- [22] K. H. Ackermann *et al.* STAR detector overview. *Nucl. Instrum. Meth.*, A499: 624–632, 2003. doi: 10.1016/S0168-9002(02)01960-5.
- [23] X. Luo and N. Xu. Search for the QCD critical point with fluctuations of conserved quantities in relativistic heavy-ion collisions at RHIC: An overview. *Nuc. Sci. Tech.*, 2017. doi: 110.1007/s41365-017-0257-0. URL <https://arxiv.org/pdf/1701.02105v3.pdf>.
- [24] L. Adamczyk *et al.* Energy dependence of moments of net-proton multiplicity distributions at RHIC. *Phys. Rev. Lett.*, 2014. doi: 10.1103/PhysRevLett.112.032302. URL <https://arxiv.org/pdf/1309.5681.pdf>.
- [25] C. Roland *et al.* Event-by-event fluctuations of particle ratios in central Pb + Pb collisions at 20-158 A GeV. *Journal of Physics G: Nuclear and Particle Physics*, 30, 2004. URL <http://stacks.iop.org/0954-3899/30/i=8/a=132>.
- [26] M. A. Stephanov. QCD critical point and event-by-event fluctuations. *Journal of Physics G: Nuclear and Particle Physics*, 533, 2011. doi: 10.1088/0954-3899/38/12/124147. URL <http://stacks.iop.org/0954-3899/38/i=12/a=124147>.
- [27] L. Adamczyk *et al.* Beam-Energy Dependence of the Directed Flow of Protons,

- Antiprotons, and Pions in Au + Au Collisions. *Phys. Rev. Lett.*, 2014. doi: 10.1103/PhysRevLett.112.162301. URL <https://arxiv.org/pdf/1401.3043.pdf>.
- [28] L. Adamczyk *et al.* Beam-energy dependence of charge separation along the magnetic field in Au+Au collisions at RHIC. *Phys. Rev. Lett.*, 113:3, 2014. URL <https://arxiv.org/pdf/1404.1433.pdf>.
- [29] L. Adamczyk *et al.* Beam-Energy Dependence of Charge Balance Functions from Au+Au Collisions at RHIC. *Phys. Rev.*, C94:4–7, 2015. URL <https://arxiv.org/pdf/1507.03539.pdf>.
- [30] The STAR Collaboration. RHIC Multi-Year Beam Use Request For Run8 - Run10, 2007. URL https://www.bnl.gov/npp/docs/pac0307/STAR_BUP_%20March_2007.pdf.
- [31] T. Abbott *et al.* Measurement of particle production in proton induced reactions at 14.6-GeV/c. *Phys. Rev.*, D45:3906–3920, 1992. doi: 10.1103/PhysRevD.45.3906.
- [32] L. Ahle *et al.* Centrality dependence of kaon yields in Si + A and Au + Au collisions at the AGS. *Phys. Rev.*, C60:044904, 1999. doi: 10.1103/PhysRevC.60.044904.
- [33] C. E. Flores. A Systematic, Large Phase Space Study of Pion, Kaon, and Proton Production in Au+Au Heavy-Ion Collisions from the RHIC Beam Energy Scan Program at STAR. *University of California Davis Dissertation*, pages 70–74, 2017. URL http://nuclear.ucdavis.edu/thesis/CEF_Thesis_Final.pdf.
- [34] H. Bichsel. A Method to Improve Tracking and Particle Identification in TPCs and Silicon Detectors. *Nuclear Instruments and Methods in Physics Research*, A562:154–197, 2006. doi: 10.1016/j.nima.2006.06.009.
- [35] W.J. Llope *et al.* The STAR Vertex Position Detector. *Nucl. Instrum. Meth.*, A759:3–5, 2014. URL <https://arxiv.org/pdf/1403.6855.pdf>.

- [36] K. C. Meehan. Pion Production in 4.5 GeV Au + Au Collisions from the STAR Fixed-Target Pilot Run. *University of California Davis Dissertation*, 2018. URL http://nuclear.ucdavis.edu/thesis/KCM_thesis_final.pdf.
- [37] Whitten Jr., C.A. and STAR Collaboration. The Beam-Beam Counter: A Local Polarimeter at STAR. In *AIP Conference Proceedings*, volume 980, page 390. American Institute of Physics, 2008.
- [38] Keane, D. TThe Beam Energy Scan at the Relativistic Heavy Ion Collider. In *Journal of Physics: Conference Series*, volume 878, page 012015. IOP Publishing, 2017.
- [39] D. Smirnov *et al.* Vertex Reconstruction at STAR: Overview and Performance Evaluation. In *Journal of Physics: Conference Series*, 898:2, 2017. URL <https://iopscience.iop.org/article/10.1088/1742-6596/898/4/042058/pdf>.
- [40] M. L. Miller *et al.* Glauber Modeling in High-Energy Nuclear Collisions. *Annual Review of Nuclear and Particle Science*, 57:205-243, 2007. doi: 10.1146/annurev.nucl.57.090506.123020. URL <https://www.annualreviews.org/doi/pdf/10.1146/annurev.nucl.57.090506.123020>.
- [41] S. Agostinelli *et al.* GEANT4 - a simulation toolkit. *Nuclear Instruments and Methods in Physics Research A*, 506:250–303, 2003. doi: 10.1016/S0168-9002(03)01368-8. URL <http://geant4.web.cern.ch/geant4/>.
- [42] F. Videbaek and O. Hansen. Baryon rapidity loss and mid-rapidity stacking in high-energy nucleus-nucleus collisions. *Phys. Rev.*, C52:2684–2693, 1995. doi: 10.1103/PhysRevC.52.2684.